

1 **A gradient tensor based subgrid scale parameterization for large-eddy**
2 **simulations of stratified shear layers using the Weather Research and**
3 **Forecasting model**

4 Sina Khani*

5 *Oden Institute for Computational Engineering and Sciences, University of Texas, Austin, TX, USA*

6 Fernando Porté-Agel

7 *Wind Engineering and Renewable Energy Laboratory (WiRE), École Polytechnique Fédérale de*
8 *Lausanne (EPFL), Lausanne, Switzerland*

9 *Corresponding author address: Oden Institute for Computational Engineering and Sciences, Uni-
10 versity of Texas at Austin, 201 E. 24th Street, Austin, TX 78712, USA
11 E-mail: sina.khani@austin.utexas.edu

ABSTRACT

12 The transition process from laminar stratified shear layer to fully developed
13 turbulence is usually captured using direct numerical simulations, in which the
14 computational cost is extremely high and the numerical domain size is limited.
15 In this work, we introduce a scale-aware subgrid scale (SGS) parameteriza-
16 tion, based on the gradient tensor of resolved variables, that is implemented
17 in the Weather Research and Forecasting (WRF) model. With this new SGS
18 model, we can skillfully resolve the characteristics of transition process, in-
19 cluding formation of vortex cores, merging vorticity billows, breaking waves
20 into smaller scales, and developing secondary instability in the stratified shear
21 layer even at coarse-resolution simulations. Our new model is developed such
22 that the time scales of the eddy viscosity and diffusivity terms are represented
23 using the tensor of gradient and not that of the rate-of-strain, which is com-
24 monly used in the parameterization of turbulent-viscosity models. We show
25 that time scales of unresolved transition processes in our new model are cor-
26 related with those of vorticity fields. At early times, the power-law slopes in
27 the kinetic and available potential energy spectra are consistent with the pro-
28 cess of formation and merging waves with an upscale energy transfer. At later
29 times, the power-law slopes are in line with the process of breaking waves
30 into small-scale motions with a downscale transfer. More importantly, the
31 efficiency of turbulent mixing is mainly high at the edge of vortex filaments
32 and not at the vortices eyes. These findings can improve our understanding of
33 turbulent mixing process in large scale wind-induced events, such as tropical
34 cyclones, using the WRF model.

³⁵ **Significance Statement**

³⁶ The evolution of instabilities in stratified shear layers has significant impacts on the structure of
³⁷ large-scale geophysical flows and also on the energy pathway to smaller-scale motions in inter-
³⁸ nal waves and turbulence. Resolving transition processes in stratified shear layers requires very
³⁹ high-resolution simulations in climate models. We propose a new subgrid-scale parameterization
⁴⁰ that is implemented in the Weather Research and Forecasting model to capture the dynamics of
⁴¹ transition process from laminar to three-dimensional turbulence in stratified shear layers at coarse-
⁴² resolution simulations. Our new scale-aware parameterization can reduce biases in climate models
⁴³ by skillfully representing unresolved fluxes, leading to higher accuracy in weather predictions of
⁴⁴ temperature, precipitation and surface fluxes with an affordable computational cost.

45 **1. Introduction**

46 Stratified shear layers are usually considered to provide the transition from laminar to turbulent
47 flows in the presence of velocity shears and density gradients (Smyth and Peltier 1990, 1993;
48 Caulfield and Peltier 2000). The evolution of stratified shear layers includes forming Kelvin-
49 Helmholtz (KH) billows and Holmboe instability, and developing secondary instabilities on the
50 edge of KH billows due to the increase of potential energy by irreversible mixing. For example,
51 turbulent KH billows with horizontal wavelength of 4 to 6 km are observed in the middle and
52 upper atmosphere above the mid-level cloud base (Luce et al. 2018). Also, coherent Gulf stream
53 rings with vorticity of diameter ~ 20 km are affected by large scale velocity shear (Leaman and
54 Molinari 1987). A pathway to smaller-scale turbulence in internal waves at the stratified ocean
55 interior is also connected to the evolution of instabilities in the stratified shear layers (Caulfield
56 and Peltier 2000; Mashayek and Peltier 2012a; Smyth and Moum 2012).

57 Most numerical simulations of stratified shear layers and KH (or Holmboe) instabilities are
58 performed using the direct numerical simulation (DNS) approach (Caulfield and Peltier 1994;
59 Scinocca 1995; Caulfield and Peltier 2000; Mashayek and Peltier 2012a; VanDine et al. 2021),
60 where a huge amount of computational resources are invested on resolving small-scale motions
61 around the molecular (viscous) dissipation scale (see e.g. Pope 2000). However, these non-
62 energetic small-scale motions around the viscous dissipation scale are not important in the tran-
63 sition process and large scale energy interactions in stratified turbulence (see e.g. Armenio and
64 Sarkar 2002; Khani and Waite 2014, 2015; Khani 2018).

65 In this paper we study the kinetic and potential energy transfers in a stratified shear layer using
66 the large-eddy simulation (LES) approach, in which the small-scale motions are not directly re-
67 solved but the effects of small scales on large-scale motions are parameterized using subgrid-scale

68 (SGS) models (see e.g. Meneveau and Katz 2000). One of the main focuses of this work is to in-
 69 troduce a new eddy viscosity model, in which the eddy time-scale of eddy viscosity (or diffusivity)
 70 coefficients are set by the gradient tensor

$$G_{ij} = \frac{\partial \bar{u}_i}{\partial x_k} \frac{\partial \bar{u}_j}{\partial x_k}, \quad (1)$$

71 rather than the strain rate tensor $s_{ij} = 1/2 (\partial \bar{u}_i / \partial x_j + \partial \bar{u}_j / \partial x_i)$, where \bar{u}_i is the resolved velocity
 72 field ($i, j = 1, 2$ and 3 ; the $\bar{\cdot}$ sign denotes resolved or filtered variable in the LES approach), and
 73 subscript k is a dummy variable (according to the Einsteins summation convention). The actual
 74 SGS momentum stress is proportional to the gradient tensor G_{ij} based on the Taylor series expan-
 75 sion of the resolved velocity field $\bar{\mathbf{u}}$ (Meneveau and Katz 2000; Khani and Porté-Agel 2017*a,b*;
 76 Khani and Waite 2020); therefore, we shall demonstrate that setting the eddy time-scale based on
 77 G_{ij} is more relevant to the structure of SGS eddies in comparison with setting an eddy time-scale
 78 based on the strain rate tensor s_{ij} , as in the Smagorinsky (1963) model. The rest of this paper is
 79 organized as follows: the governing equations for the stratified shear layer simulations, along with
 80 our new SGS model are introduced in section 2. Section 3 gives the methodology and simulations
 81 setup. Results and discussion are given in section 4, followed by conclusions in section 5.

82 2. Governing equations

83 The non-dimensional governing equations of motion under the Boussinesq approximation are
 84 given as follows

$$\frac{\partial \bar{u}_i}{\partial t} + \frac{\partial}{\partial x_j} (\bar{u}_i \bar{u}_j) = - \frac{\partial \bar{p}}{\partial x_i} + \text{Ri} \bar{\theta} \mathbf{e}_z + \frac{1}{\text{Re}} \nabla^2 \bar{u}_i - \frac{\partial \tau_{ij}}{\partial x_j}, \quad (2)$$

$$\frac{\partial \bar{u}_i}{\partial x_i} = 0, \quad (3)$$

$$\frac{\partial \bar{\theta}}{\partial t} + \frac{\partial}{\partial x_j} (\bar{\theta} \bar{u}_j) + \bar{w} = \frac{1}{\text{RePr}} \nabla^2 \bar{\theta} - \frac{\partial h_j}{\partial x_j}, \quad (4)$$

where $\bar{\mathbf{u}} = (\bar{u}, \bar{v}, \bar{w})$, $\bar{\theta}$, \bar{p} are the filtered (resolved) velocity, potential temperature and pressure;
 $\text{Ri} = gd\delta\theta / (\mathcal{U}^2\theta_0)$ is the bulk Richardson number, $\text{Re} = \mathcal{U}d/\nu$ is the Reynolds number and
 $\text{Pr} = \nu/D$ is the Prandtl number. Here, d , $\delta\theta$, \mathcal{U} , θ_0 , ν and D are the initial thickness of shear
 layer, potential temperature deviation, velocity scale, reference potential temperature, molecular
 viscosity and diffusivity coefficients, respectively. The SGS momentum flux τ_{ij} and potential tem-
 perature flux h_j need to be parameterized using SGS models. In LES, we mainly resolve scales
 much larger than the Kolmogorov (Batchelor) scale, leading to neglect the molecular viscosity
 (diffusivity) dissipations in comparison with the SGS dissipations by the eddy viscosity (diffusiv-
 ity).

a. Parameterizing eddy viscosity and diffusivity terms

The SGS momentum flux τ_{ij} can be approximated by a Taylor series expansion of the resolved
 velocity field $\bar{\mathbf{u}}$ at a point \mathbf{x} over a distance \mathbf{r} , where $|\mathbf{r}| \sim \Delta$, which is the filter width (grid spacing)
 in the LES approach (Pope 2000; Meneveau and Katz 2000; Khani and Porté-Agel 2017*b*; Khani
 and Waite 2020)

$$\tau_{ij} \approx \frac{\Delta^2}{12} G_{ij} = \frac{\Delta^2}{12} \frac{\partial \bar{u}_i}{\partial x_k} \frac{\partial \bar{u}_j}{\partial x_k}. \quad (5)$$

However, a SGS model based on the equation (5) cannot provide enough dissipation at scales
 around the grid spacing Δ (as discussed in Vreman et al. 1997; Khani and Porté-Agel 2017*a,b*). In
 order to take advantage of the high correlation between the gradient tensors and SGS fluxes, we
 suggest an eddy viscosity model to parameterize τ_{ij} as follows

$$\tau_{ij} = -2\nu_g s_{ij}, \quad (6)$$

¹⁰³ where v_g uses the structure of G_{ij} instead of s_{ij} that is used in the Smagorinsky model. In our new
¹⁰⁴ parameterization, the eddy viscosity coefficient v_g is proposed as

$$v_g = c_g \Delta^2 (G_{ij} G_{ij})^{1/4}, \quad (7)$$

¹⁰⁵ which is different from the eddy viscosity coefficient in the Smagorinsky parameterization with
¹⁰⁶ $v_g = c_s \Delta^2 (s_{ij} s_{ij})^{1/2}$. Here, c_g and c_s are model coefficients. The novelty of our new model is
¹⁰⁷ that we employ the gradient tensor, which provides a theoretical approximation of the actual SGS
¹⁰⁸ tensor, in the definition of the eddy viscosity coefficient v_g . The advantage of our new SGS model
¹⁰⁹ compared to the Smagorinsky model is that the eddy viscosity coefficient in our model includes
¹¹⁰ the structure of the gradient tensor, which has been shown to be highly correlated with the actual
¹¹¹ SGS motions (see e.g. Clark et al. 1979; Pope 2000; Porté-Agel et al. 2001; Khani and Porté-Agel
¹¹² 2017a). Overall, our new model is as simple as the Smagorinsky model but it sets the eddy time-
¹¹³ scale based on a theoretical approximation of the gradient tensor G_{ij} , and not the rate of strain
¹¹⁴ tensor s_{ij} .

¹¹⁵ In theory, our SGS eddy viscosity coefficient in equation (7) sets the eddy turnover time-scale
¹¹⁶ using the gradient tensor, which mathematically approximates the actual SGS motions using the
¹¹⁷ Taylor series expansion of the resolved velocity field (see equation 5). We propose this new model
¹¹⁸ as an alternative to the Smagorinsky model because the Smagorinsky model is too dissipative to
¹¹⁹ simulate overturning and transition to turbulence (Vreman et al. 1997; Khani and Waite 2015). A
¹²⁰ theoretical value is obtained for the constant coefficient c_g using an isotropic inertial subrange for
¹²¹ the kinetic energy spectrum (as shown in Appendix A).

¹²² The eddy diffusivity term h_j in our new model is parameterized as follows

$$h_j = -D_g \frac{\partial \bar{\theta}}{\partial x_j}, \quad (8)$$

¹²³ where $D_g = v_g / Pr_t$, and Pr_t is the SGS Prandtl number.

124 **3. Methodology**

125 We consider idealized simulations using the Weather Research and Forecasting (WRF-LES)
126 model to study stratified shear layers. The WRF model uses a hydrostatic-pressure vertical co-
127 ordinate, and also includes a rotating term with the Coriolis parameter $f_c = 10^{-4} \text{ s}^{-1}$ (in our
128 simulations, the effects of Coriolis parameter on the evolution and transition of shear layers are
129 negligible since the computational domain is small enough to have a fairly large Rossby num-
130 ber). Free-slip boundaries are imposed at the top and bottom surfaces and lateral directions have
131 periodic boundary conditions. The third-order Runge-Kutta scheme is employed for the time ad-
132 vancement; fifth- and third-order upwind biased finite difference methods are also employed for
133 the spatial discretization in the horizontal and vertical directions, respectively. The initial stream-
134 wise velocity and potential temperature profiles are given as follows (similar initialization is used
135 in Smyth and Peltier 1990, 1993; Caulfield and Peltier 2000; Mashayek and Peltier 2012a)

$$\bar{u}(z, t = 0) = \mathcal{U} \tanh\left(\frac{z - H}{d}\right), \quad (9)$$

$$\bar{\theta}(z, t = 0) - \theta_0 = \delta\theta \tanh\left(\frac{z - H}{d}\right), \quad (10)$$

136 where H is the half-height of the computational domain.

137 Eight simulations are performed using our newly developed SGS parameterization. Simulations
138 are characterized with different initial bulk Richardson number Ri , half shear layer thickness d , and
139 velocity scale \mathcal{U} ; simulations are also run at different resolutions with grid points $n_x \times n_y \times n_z =$
140 $80 \times 80 \times 80$, $160 \times 160 \times 160$, and $320 \times 320 \times 320$ over a cubic domain where \mathcal{L}_x and \mathcal{L}_y are
141 integer multiples of the most unstable KH modes (Hazel 1972), and $\mathcal{L}_z = 2 \text{ [km]}$. For runs # 3-6
142 where the horizontal domain is reduced, n_x and n_y are 230. The SGS Prandtl number is set to 1/3
143 (similar to Skamarock et al. 2008). Table 1 shows a list of parameters and variables in our LES
144 runs. Flow structures and dynamics at coarser resolution simulations are similar to those at high-

¹⁴⁵ resolution runs, but there is less clarity on capturing fundamental processes in coarse-resolution
¹⁴⁶ simulations with $n_{x,y,z} = 160^3$ and 80^3 grid points; hence, in this work we mainly focus on the
¹⁴⁷ results of high-resolution cases with $n_{x,y,z} = 320^3$ and $n_{x,y,z} = 230^2 \times 320$ grid points.

¹⁴⁸ 4. Results and discussion

¹⁴⁹ a. Vorticity fields

¹⁵⁰ Figure 1 shows time evolution of the y -direction vorticity field in the x - z plane for the case with
¹⁵¹ the initial bulk Richardson number $Ri = 0.041$ and shear layer thickness $d = 25$ [m] (i.e. run # 1 in
¹⁵² Table 1). At $t = 0$, the shear layer is thin and approximately steady (not shown). As time evolves,
¹⁵³ intermittency grows and we can see the onset of KH instability at $t = 75$ [s]. At $t = 105$ [s], a train
¹⁵⁴ of four KH vorticity cores (billows) is formed, and these vortex cores are connected by vorticity
¹⁵⁵ filaments (braids). The vorticity cores start merging at $t = 135$ [s] and two vorticity billows are
¹⁵⁶ formed, and breaking KH waves into smaller-scale structures (turbulence) occurs at $t = 195$ [s]. At
¹⁵⁷ later times, the process of merging vorticity cores and breaking waves into turbulence, along with
¹⁵⁸ developing secondary instability that enhances turbulence collapse in the mixing layer, are seen
¹⁵⁹ (figures 1e and 1f). The occurrence of secondary instability mostly emerges along braids when the
¹⁶⁰ vorticity cores merge, and also at the edge of KH billows (as shown in figures 1e–g). At $t = 615$ [s],
¹⁶¹ the process of transition into turbulence has mostly completed and small-scale vorticity structures
¹⁶² and filaments are mainly visible. These structures and processes are in line with those reported
¹⁶³ in the literature on the formation of KH waves and three-dimensional evolution into turbulence
¹⁶⁴ (Corcos and Sherman 1976; Smyth and Peltier 1991, 1993; Staquet 1995, 2000; Caulfield and
¹⁶⁵ Peltier 2000; Smyth 2003, 2004; Mashayek and Peltier 2012a,b; Fritts et al. 2014).

166 Next, we increase the initial shear layer thickness to $d = 50$ [m], thereby the bulk Richardson
167 number $Ri = 0.082$ is doubled (run # 2 in Table 1). In this case, the processes of KH billow
168 formation, breaking waves and transition into turbulence delay over time in comparison with those
169 in run # 1. In the case with the initial bulk Richardson number $Ri = 0.082$ and shear layer thickness
170 $d = 50$ [m], a train of three vorticity cores has emerged by $t = 195$ [s] (figure 2a). At $t = 255$ [s],
171 vorticity cores merge into two billows while KH waves start breaking into small-scale structures
172 and the secondary instability develops across the braids of KH vortices (as shown in figure 2b;
173 see also figure 2c, where breaking KH waves and secondary instabilities are well captured at
174 $t = 285$ [s]). Ultimately, small-scale vorticity filaments and enlarged shear layer thickness are
175 seen at $t = 465$ [s] (figure 2d). It is also important to note that the intensity of vorticity filaments
176 attenuates at later time due to the effect of SGS eddy dissipation on smaller scales (as shown in
177 figure 2d). Time evolution of the y -direction vorticity field ω_y in the x - y and y - z planes is shown in
178 figure 3. Small-scale instabilities emerge in the y -direction at a time around $t = 195$ [s] (figures 3a
179 and 3b). These instabilities grow over time during the waves breaking process in three dimensions
180 (figures 3c and 3d at $t = 255$ [s]). As time evolves, small-scale instabilities further grow during
181 the process of merging billows and formation of secondary instability at time $t = 285$ [s] (figures
182 3e and 3f). Overall, these results demonstrate that the transition from laminar stratified shear
183 layer to fully developed turbulence includes the wave breaking, merging billows and formation of
184 secondary instability through a 3D process (figures 2 and 3).

185 For a case with the initial bulk Richardson number $Ri = 0.164$ and shear layer thickness $d = 100$
186 [m], breaking KH waves and formation of secondary instabilities along vorticity braids are seen
187 at $t = 585$ [s] (figure 4a). It is noteworthy that secondary KH billows are formed at scales that
188 are mainly smaller than the scale of the first-generation KH waves (see figure 4b). Interestingly,
189 secondary KH billows may evolve over time towards breaking secondary waves, turbulence oc-

190 currence, and even merging with larger-scale KH billows (these processes are similar to those are
191 captured in breaking the first generation KH waves; see figures 4b and 4c). For the case with
192 the initial bulk Richardson number $Ri = 0.197$ and layer thickness $d = 100$ [m], the shear layer
193 evolves to form Holmboe-like waves at $t = 765$ [s] (figure 5a; similar wave structures are reported
194 in DNS of Smyth and Winters 2003). In this case, the thickness of the mixing layer is shallower
195 than previous cases in which the initial bulk Richardson number and shear layer thickness were
196 smaller. Furthermore, the formation of Holmboe waves delayed in the case with $Ri = 0.235$ and
197 $d = 100$ [m] (figure 5b). As elaborated in Salehipour et al. (2016), Holmboe waves grow slowly
198 over time and they scour (versus KH waves overturn) as time evolves by exhibiting a $-5/3$ power-
199 law in the kinetic energy spectra with an energy level that is relatively smaller than that in KH
200 waves (see figure 9 in section b). If we further increase the initial bulk Richardson number to
201 $Ri = 0.327$, the emergence of instability and waves is suppressed (not shown) because Ri becomes
202 larger than the *critical* bulk Richardson number $Ri_{cr} = 1/4$, which is a necessary condition for
203 instability growth in stratified shear layers (Miles 1961; Peltier and Caulfield 2003).

204 *b. Energy spectra*

205 Figure 6 shows the time evolution of vertically-averaged horizontal wavenumber kinetic and
206 available potential energy (KE and APE) spectra within the stratified shear layer for the case
207 with $Ri = 0.041$ and $d = 25$ [m]. At $t = 105$ and 135 [s], when KH waves are formed and the
208 merging process occurs, KE and APE spectra are dominated by peaks at the wavenumbers of KH
209 harmonics. The APE spectra are more energetic at early times in comparison with KE spectra,
210 and the spectral slope of kinetic energy is close to -3 (a sign of upscale energy transfer because
211 of formation and merging KH waves; see figures 6a and 6b). As time evolves, at $t = 195$ [s]
212 a time which three-dimensionalization occurs where KH waves start breaking, the KE and APE

213 spectra show similar energy levels at large horizontal scales (small wavenumbers), and the spectral
214 slopes become closer to $-5/3$ over the range of intermediate horizontal wavenumbers (a sign of
215 downscale energy transfer because of breaking waves into smaller structures; see figures 6c and
216 6d). As time further evolves, the KE spectra become more energetic in comparison with those
217 of APE and a clear $-5/3$ spectral power law is visible (down-scale cascade of energy by onset
218 of turbulence; see figures 6e and 6f). At later times, SGS eddy dissipation increases due to the
219 onset of turbulence (see section c); hence, the energy levels of KE and APE spectra are remarkably
220 decreased (figure 6g).

221 Similar trends are seen in the case with $Ri = 0.082$ and $d = 50$ [m], for which the energy spectra
222 at $t = 195$ [s] include wavenumber peaks of KH waves, and show domination of APE because
223 of the merging process and formation of KH billows with a spectral slope ~ -3 (see figure 7a).
224 At later times however, KE levels become gradually larger than APE levels with a spectral slope
225 $\sim -5/3$ (figures 7b–e). Also, KE and APE levels significantly decrease due to the SGS eddy
226 dissipation on smaller scales at later times (see figure 7e when $t = 735$ [s]). For the case with the
227 initial bulk Richardson number $Ri = 0.164$ and shear layer thickness $d = 100$ [m], spectral shapes
228 are similar to those we reported in figures 6 and 7 (see figures 8a and 8b; consistent with the time
229 delay on formation and merging KH waves, and turbulence onset that are discussed in section a).
230 In the case with the initial bulk Richardson number $Ri = 0.197$ and $d = 100$ [m], the KE and APE
231 spectra show (less-energetic) wavenumber peaks and harmonics at $t = 585$ [s] when Holmboe like
232 waves start forming (figure 9a). At the later time $t = 885$ [s], energy spectra are more smooth
233 and depict a $-5/3$ spectra power law due to turbulence occurrence and breaking Holmboe waves
234 into smaller-scale structures (figure 9b). For the case with $Ri = 0.235$ and $d = 100$ [m], the KE
235 and APE spectra show the wave harmonics at very late times (for example, Holmboe instability
236 in this case occurs at around $t = 825$ [s]; not shown). Moreover, the process of breaking waves

237 into turbulence, with a $-5/3$ power spectra, are also seen at $t = 1005$ [s] in this case (delayed
238 instability formation and downscale transfer of energy; not shown).

239 *c. Shear characteristics and dissipation rates*

240 Figure 10 shows the time evolution of resolved shear (filtered shear characteristics) $\bar{S} =$
241 $(G_{ij}G_{ij})^{1/4}$ in the x - z plane for the case with the initial bulk Richardson number $Ri = 0.041$
242 and shear layer thickness $d = 25$ [m]. From figures 1 and 10, it is suggestive that the resolved
243 shear \bar{S} and vorticity field ω_y are highly correlated. Figure 11 shows a scatter diagram of ω_y versus
244 \bar{S} at different times for the case with $Ri = 0.041$ and $d = 25$ [m]. At early time, when primary
245 KH billows start emerging, ω_y is well approximated by \bar{S} with a correlation coefficient around 1
246 ($\omega_y \approx \bar{S}$ as shown in figure 11a). As time evolves, where waves breaking occurs and secondary
247 instability starts forming, the nonlinearity becomes dominant due to the onset of turbulence; hence
248 the correlation coefficient between ω_y and \bar{S} varies from -1 to 1 ($-\bar{S} \lesssim \omega_y \lesssim \bar{S}$, see figures 11b–d).
249 Time scales of KH billows, merging processes, breaking waves and turbulence onset in vorticity
250 field are better correlated with those of filtered shear characteristics because the time scale of SGS
251 stress τ_{ij} is proportional to \bar{S} and s_{ij} , and \bar{S} is computed from G_{ij} in the gradient model. Moreover,
252 our work shows that the eddy viscosity coefficient in this new definition of \bar{S} is less-dissipative in
253 the region with high shears in comparison with the regular Smagorinsky model (see section e).

254 Figures 12 and 13 show the time evolution of kinetic and potential SGS eddy dissipation rates ε
255 and ε_p , respectively, in the x - z plane. When turbulence onsets at $t \approx 195$ [s], SGS eddy dissipation
256 rates depict maximum values at vorticity filaments and smaller-scale structures. It is shown that
257 the SGS potential eddy dissipation rate ε_p is much larger than the SGS kinetic eddy dissipation
258 rate ε at vorticity braids and wave edges, while ε is mostly dominant at vorticity cores (as shown
259 in figures 12 and 13; in particular, see figures 12d–g and figures 13d–g). Similar trends are also

260 shown in the case with $\text{Ri} = 0.082$ and $d = 50$ [m], where the shear characteristics \bar{S} can correctly
261 predict the transition of stratified shear layer from KH billow formation to breaking waves and
262 the occurrence of turbulence (figures 14a–c). The time evolution of kinetic and potential eddy
263 dissipation rates shows the transition process where maximum values of ε occur at vorticity cores
264 while ε_p shows maximum values at vorticity braids and filaments (see figures 15a–d).

265 For the case with the initial bulk Richardson number $\text{Ri} = 0.164$ and shear layer thickness $d =$
266 100 [m], the SGS kinetic and potential eddy dissipation rates show peak values where both primary
267 KH wave and secondary instability are formed. As shown in figures 16a and 16b, ε and ε_p are
268 mainly dominant at vortex eyes and braids of the first (and also secondary) wave(s), respectively.
269 The SGS potential eddy dissipation rate ε_p is more dominant at braids of Holmboe vorticities in
270 the case with $\text{Ri} = 0.197$ and $d = 100$ [m] (figures 17a and 17b). These trends are consistent with
271 the time evolution of ε_p over x - z plane for KH waves we discussed above (see figure 13).

272 *d. Mixing efficiency*

273 Mixing efficiency, which is defined as a measure of the effectiveness of turbulence in mixing
274 process, is an important microscale parameter that influences breaking gravity waves and verti-
275 cal transport of heat and tracers in atmospheric shear layers (Lilly et al. 1974; Weinstock 1978;
276 Caulfield and Peltier 2000). In the LES approach, the irreversible mixing efficiency γ_i is defined
277 as the ratio of SGS potential eddy dissipation ε_p to the total SGS dissipation ($\varepsilon_p + \varepsilon$) as follows
278 (Khani 2018)

$$\gamma_i = \frac{\varepsilon_p}{\varepsilon_p + \varepsilon}. \quad (11)$$

279 Figure 18 shows the time evolution of γ_i in the x - z plane. Interestingly, the irreversible mixing
280 efficiency is more effective at the edge of vorticity filaments and braids where the SGS potential

281 dissipation rate is maximum, while the efficiency of turbulent mixing is weaker at vorticity cores
282 (see figures 18a–d). Similar structures are also seen in our cases with different initial Richard-
283 son numbers and shear layer thicknesses where KH and Holmboe waves are formed (not shown).
284 These results demonstrate that the irreversible turbulent mixing is mainly influential at vorticity
285 filaments and braids rather than vorticity cores (eyes). Small values of mixing efficiency at vor-
286 ticity cores, where waves breaking occurs, is due to small ratio of potential to kinetic energy eddy
287 dissipation (i.e. $\varepsilon_p/\varepsilon \ll 1$) because in this scenario $\gamma_i \approx \varepsilon_p/\varepsilon$ (see equation 11). Our results are in
288 line with those from Gassmann (2018) that the thermal dissipation is much smaller than the kinetic
289 energy dissipation in numerical experiments of breaking gravity waves. These findings can be use-
290 ful for better understanding the interactive mixing in large-scale motions of tropical cyclones, in
291 which mixing is mainly carried by transient wind-driven events at low local Richardson numbers
292 (i.e. turbulent mixing) rather than mixing by diffusion (as discussed in Raymond et al. 2004; Korty
293 et al. 2008).

294 e. Comparison with the Smagorinsky parameterization

295 We have performed an extra LES run with the Smagorinsky parameterization in order to compare
296 the results of our newly implemented SGS model in WRF-LES code with those from the existing
297 SGS model. We consider the case with the initial bulk Richardson number $Ri = 0.164$ and shear
298 layer thickness 100 [m] in the LES run with the Smagorinsky model. The stratified shear layer
299 is stable until $t = 945$ [s], a time which instabilities start growing, and also the formation of KH
300 instabilities emerges at $t \approx 1125$ [s] (figures 19a and 19b). With the gradient model, however, this
301 case shows breaking waves and formation of secondary instabilities at $t \approx 585$ [s] (as was shown
302 in figure 4a). As a result, the evolution time of stratified shear layer and transition processes
303 are significantly postponed because, unlike the gradient model, the Smagorinsky model is too

304 dissipative and excessive eddy dissipation does not allow the growth of instabilities and formation
305 of primary and secondary instabilities at an early time. Similar trends are also shown in the kinetic
306 and potential energy dissipation rates ε and ε_p , where the onset of turbulence is suppressed at early
307 time in the LES run with the Smagorinsky parameterization. In fact, the formation of KH billows
308 and merging processes in this case are delayed until $t \approx 1185$ [s] when the Smagorinsky model is
309 employed (see figures 19c and 19d).

310 5. Conclusion

311 In this work we implement a new SGS parameterization, in which the eddy time scale of un-
312 resolved fluxes is set by the gradient tensor G_{ij} , for LES of stratified shear layers in the WRF
313 model. We test our new model in cases with different initial bulk Richardson number and layer
314 thicknesses. Using coarse-resolution WRF-LES runs, we could capture the formation of vorticity
315 cores, merging vorticity billows, breaking waves into small-scale structures and development of
316 secondary instability. Usually, very high-resolution DNS runs are required to capture the transition
317 process from laminar shear layer to fully developed three-dimensional turbulence (as are shown
318 in e.g. Smyth 2003; Smyth and Winters 2003; Smyth 2004; Mashayek and Peltier 2012a,b).
319 Here, we have shown that these fundamental dynamics of stratified shear layers can be skillfully
320 captured in coarse-resolution LES runs when a scale-aware SGS parameterization based on the
321 gradient tensor is employed.

322 The power-law of KE and APE spectra changes over time in this transition process: a -3 spectral
323 slope for upscale energy transfer is seen at early stages due to the formation and merging KH
324 waves (or Holmboe instability when Ri is large but still $\lesssim Ri_{cr}$), while a $-5/3$ spectral slope for
325 down-scale energy transfer is captured at later times associated with breaking waves into small-
326 scale motions (figures 6 and 7). Furthermore, time scales of SGS transition processes, which are

327 indicated by the filtered shear characteristics $\bar{S} = (G_{ij}G_{ij})^{1/4}$ can lead to set in a less-dissipative
328 correlation coefficient in the eddy viscosity model. It is remarkable that the SGS potential eddy
329 dissipation rate ε_p is large at the leading edges of waves (instabilities) and vorticity braids whereas
330 the SGS kinetic eddy dissipation rate ε is mostly effective at vorticity cores (figures 12 and 13).
331 As a result, the efficiency of turbulent mixing, which is carried by wind-driven events at low Ri
332 values, is mainly important at vorticity braids and filaments and not at the vortex eyes (equation
333 11 and figure 18).

334 The new SGS parameterization based on the gradient tensor is useful in high-resolution numeri-
335 cal weather prediction models to enhance the performance of eddy viscosity (diffusivity) parame-
336 terizations for boundary layer processes, convection and cloud dynamics. Since SGS fluxes in the
337 gradient-based parameterization are less-diffusive, modeling unresolved processes, potential tem-
338 perature, precipitation, air-sea fluxes and other meteorological elements shall be predicted with
339 higher accuracy in high-resolution weather forecasting models. For future work, we will employ
340 our new gradient-based SGS parameterization in numerical simulations of tropical cyclones and
341 hurricane predictions using the WRF model (similar work with current microphysics parameteri-
342 zations has been done in WRF-LES and Cloud Model 1; see Zhu 2008; Nolan et al. 2017).

343 6. Acknowledgement

344 This work has benefited from comments by Michael Waite and three anonymous review-
345 ers. Computing resources from Scientific IT and Application Support (SCITAS) at École Poly-
346 technique Fédérale de Lausanne (EPFL) are acknowledged. Model data and source code for
347 generating the results can be accessible from the GitHub (<https://github.com/sinakhani/Stratified-shear-layer-in-WRF>).
348

APPENDIX A

A theoretical approach to determine c_g

351 According to equations (6) and (7), the subgrid stress tensor τ_{ij} can be written as follows

$$\tau_{ij} = c_g \Delta^2 (G_{kl} G_{kl})^{1/4} s_{ij}, \quad (\text{A1})$$

352 and therefore, the dissipation rate $\varepsilon = \tau_{ij} s_{ij}$ is given in the following form

$$\varepsilon = c_g \Delta^2 (G_{kl} G_{kl})^{1/4} s_{ij} s_{ij}. \quad (\text{A2})$$

353 We can write the resolved gradient and strain-rate terms $G_{ij} G_{ij}$ and $s_{ij} s_{ij}$, respectively, in the

354 Fourier space (see e.g. Pope 2000)

$$G_{ij} G_{ij} \approx 4 \left(\int k^2 \mathcal{G}^2(k) E(k) dk \right) \left(\int k^2 \mathcal{G}^2(k) E(k) dk \right), \quad (\text{A3})$$

$$s_{ij} s_{ij} = 2 \int k^2 \mathcal{G}(k) E(k) dk, \quad (\text{A4})$$

355 where $\mathcal{G}(k)$ and $E(k)$ are the filter function and kinetic energy spectrum, respectively. Assum-

356 ing that $\mathcal{G}(k)$ is the cutoff filter function with the cutoff wavenumber $k_c = \pi/\Delta$, and $E(k) =$

357 $\mathcal{C} \varepsilon^{2/3} k^{-5/3}$ is the isotropic Kolmogorov inertial subrange, equations (A3-A4) can be simplified:

$$G_{ij} G_{ij} \approx 4 \mathcal{C}^2 \varepsilon^{4/3} \left(\frac{3}{4} \right)^2 \left(\frac{\pi}{\Delta} \right)^{8/3}, \quad (\text{A5})$$

$$s_{ij} s_{ij} \approx 2 \mathcal{C} \varepsilon^{2/3} \left(\frac{3}{4} \right) \left(\frac{\pi}{\Delta} \right)^{4/3}. \quad (\text{A6})$$

358 Here, \mathcal{C} is a constant coefficient (we are aware that turbulent flows are highly anisotropic in atmo-

359 spheric sciences. The isotropic Kolmogorov subrange is only a primitive assumption to develop a

360 theoretical approach for estimating the correlation coefficient c_g in the gradient model). Substitut-

361 ing equations (A5-A6) into equation (A2) results in

$$\varepsilon = c_g \Delta^2 \left[\left(\frac{3}{2} \right)^{3/2} \mathcal{C}^{3/2} \varepsilon \left(\frac{\pi}{\Delta} \right)^2 \right], \quad (\text{A7})$$

362 from which we can obtain a theoretical estimate for c_g in the following form

$$c_g = \frac{(2/3)^{3/2}}{\mathcal{C}^{3/2}\pi^2}. \quad (\text{A8})$$

363 If we use $\mathcal{C} = 1.51$ (as is suggested in Pope 2000; Meneveau and Katz 2000), c_g can be estimated
364 as follows

$$c_g = 0.0299, \quad (\text{A9})$$

365 which is interestingly close to the Smagorinsky coefficient $c_s^2 = (0.17)^2 = 0.0289$. The similarity
366 of c_g and c_s^2 is left for the future investigation.

367 References

- 368 Armenio, V. and Sarkar, S. (2002), ‘An investigation of stably stratified turbulent channel flow
369 using large-eddy simulation’, *Journal of Fluid Mechanics* **459**, 1.
- 370 Caulfield, C. and Peltier, W. (1994), ‘Three dimensionalization of the stratified mixing layer’,
371 *Physics of Fluids* **6**(12), 3803–3805.
- 372 Caulfield, C. and Peltier, W. (2000), ‘The anatomy of the mixing transition in homogeneous and
373 stratified free shear layers’, *Journal of Fluid Mechanics* **413**, 1–47.
- 374 Clark, R. A., Ferziger, J. H. and Reynolds, W. C. (1979), ‘Evaluation of subgrid-scale models
375 using an accurately simulated turbulent flow’, *Journal of Fluid Mechanics* **91**(1), 1–16.
- 376 Corcos, G. M. and Sherman, F. S. (1976), ‘Vorticity concentration and the dynamics of unstable
377 free shear layers’, *Journal of Fluid Mechanics* **73**(2), 241–264.
- 378 Fritts, D. C., Wan, K., Werne, J., Lund, T. and Hecht, J. H. (2014), ‘Modeling the implications
379 of Kelvin–Helmholtz instability dynamics for airglow observations’, *Journal of Geophysical
380 Research: Atmospheres* **119**(14), 8858–8871.

- 381 Gassmann, A. (2018), ‘Entropy production due to subgrid-scale thermal fluxes with application to
382 breaking gravity waves’, *Quarterly Journal of the Royal Meteorological Society* **144**(711), 499–
383 510.
- 384 Hazel, P. (1972), ‘Numerical studies of the stability of inviscid stratified shear flows’, *Journal of*
385 *Fluid Mechanics* **51**(1), 39–61.
- 386 Khani, S. (2018), ‘Mixing efficiency in large-eddy simulations of stratified turbulence’, *Journal of*
387 *Fluid Mechanics* **849**, 373–394.
- 388 Khani, S. and Porté-Agel, F. (2017a), ‘Evaluation of non-eddy viscosity subgrid-scale models
389 in stratified turbulence using direct numerical simulations’, *European Journal of Mechanics-*
390 *B/Fluids* **65**, 168–178.
- 391 Khani, S. and Porté-Agel, F. (2017b), ‘A modulated-gradient parametrization for the large-eddy
392 simulation of the atmospheric boundary layer using the weather research and forecasting
393 model’, *Boundary-Layer Meteorology* **165**(3), 385–404.
- 394 Khani, S. and Waite, M. (2014), ‘Buoyancy scale effects in large-eddy simulations of stratified
395 turbulence’, *Journal of Fluid Mechanics* **754**, 75.
- 396 Khani, S. and Waite, M. L. (2015), ‘Large eddy simulations of stratified turbulence: The dynamic
397 smagorinsky model’, *Journal of Fluid Mechanics* **773**(327-344), 480.
- 398 Khani, S. and Waite, M. L. (2020), ‘An anisotropic subgrid-scale parameterization for large-eddy
399 simulations of stratified turbulence’, *Monthly Weather Review* **148**(10), 4299–4311.
- 400 Korty, R. L., Emanuel, K. A. and Scott, J. R. (2008), ‘Tropical cyclone-induced upper-ocean
401 mixing and climate: Application to equable climates’, *Journal of Climate* **21**(4), 638–654.

- 402 Leaman, K. D. and Molinari, R. L. (1987), ‘Topographic modification of the florida current by
403 little bahama and great bahama banks’, *Journal of Physical Oceanography* **17**(10), 1724–1736.
- 404 Lilly, D., Waco, D. and Adelfang, S. (1974), ‘Stratospheric mixing estimated from high-altitude
405 turbulence measurements’, *Journal of Applied Meteorology and Climatology* **13**(4), 488–493.
- 406 Luce, H., Kantha, L., Yabuki, M. and Hashiguchi, H. (2018), ‘Atmospheric kelvin–helmholtz bil-
407 lows captured by the mu radar, lidars and a fish-eye camera’, *Earth, Planets and Space* **70**(1), 1–
408 15.
- 409 Mashayek, A. and Peltier, W. (2012a), ‘The ‘zoo’of secondary instabilities precursory to stratified
410 shear flow transition. Part 1 shear aligned convection, pairing, and braid instabilities’, *Journal
411 of Fluid Mechanics* **708**, 5.
- 412 Mashayek, A. and Peltier, W. (2012b), ‘The ‘zoo’of secondary instabilities precursory to stratified
413 shear flow transition. Part 2 the influence of stratification’, *Journal of Fluid Mechanics* **708**, 45.
- 414 Meneveau, C. and Katz, J. (2000), ‘Scale-invariance and turbulence models for large-eddy simu-
415 lation’, *Annual Review of Fluid Mechanics* **32**(1), 1–32.
- 416 Miles, J. W. (1961), ‘On the stability of heterogeneous shear flows’, *Journal of Fluid Mechanics*
417 **10**(4), 496–508.
- 418 Nolan, D. S., Dahl, N. A., Bryan, G. H. and Rotunno, R. (2017), ‘Tornado vortex structure, inten-
419 sity, and surface wind gusts in large-eddy simulations with fully developed turbulence’, *Journal
420 of the Atmospheric Sciences* **74**(5), 1573–1597.
- 421 Peltier, W. and Caulfield, C. (2003), ‘Mixing efficiency in stratified shear flows’, *Annual Review
422 of Fluid Mechanics* **35**(1), 135–167.

- 423 Pope, S. B. (2000), ‘Turbulent flows, pp 558–638’.
- 424 Porté-Agel, F., Parlange, M. B., Meneveau, C. and Eichinger, W. E. (2001), ‘A priori field study
425 of the subgrid-scale heat fluxes and dissipation in the atmospheric surface layer’, *Journal of the*
426 *Atmospheric Sciences* **58**(18), 2673–2698.
- 427 Raymond, D. J., Esbensen, S. K., Paulson, C., Gregg, M., Bretherton, C. S., Petersen, W. A.,
428 Cifelli, R., Shay, L. K., Ohlmann, C. and Zuidema, P. (2004), ‘Epic2001 and the coupled ocean–
429 atmosphere system of the tropical east pacific’, *Bulletin of the American Meteorological Society*
430 **85**(9), 1341–1354.
- 431 Salehipour, H., Caulfield, C.-c. and Peltier, W. (2016), ‘Turbulent mixing due to the holmboe wave
432 instability at high reynolds number’, *Journal of Fluid Mechanics* **803**, 591–621.
- 433 Scinocca, J. (1995), ‘The mixing of mass and momentum by kelvin-helmboltz billows’, *Journal*
434 *of Atmospheric Sciences* **52**(14), 2509–2530.
- 435 Skamarock, W. C., Klemp, J. B., Dudhia, J., Gill, D. O., Barker, D. M., Wang, W. and Powers,
436 J. G. (2008), ‘A description of the advanced research wrf version 3. ncar technical note-475+
437 str’.
- 438 Smagorinsky, J. (1963), ‘General circulation experiments with the primitive equations: I. the basic
439 experiment’, *Monthly Weather Review* **91**(3), 99–164.
- 440 Smyth, W. D. (2003), ‘Secondary Kelvin–Helmholtz instability in weakly stratified shear flow’,
441 *Journal of Fluid Mechanics* **497**, 67–98.
- 442 Smyth, W. D. (2004), ‘Kelvin–Helmholtz billow evolution from a localized source’, *Quarterly*
443 *Journal of the Royal Meteorological Society: A Journal of the Atmospheric Sciences, Applied*
444 *Meteorology and Physical Oceanography* **130**(603), 2753–2766.

- 445 Smyth, W. D. and Moum, J. N. (2012), ‘Ocean mixing by kelvin-helmholtz instability’, *Oceanography*
446 **25**(2), 140–149.
- 447 Smyth, W. and Peltier, W. (1990), ‘Three-dimensional primary instabilities of a stratified, dissipative,
448 parallel flow’, *Geophysical & Astrophysical Fluid Dynamics* **52**(4), 249–261.
- 449 Smyth, W. and Peltier, W. (1991), ‘Instability and transition in finite-amplitude KelvinHelmholtz
450 and Holmboe waves’, *Journal of Fluid Mechanics* **228**, 387–415.
- 451 Smyth, W. and Peltier, W. (1993), ‘Two-dimensional turbulence in homogeneous and stratified
452 shear layers’, *Geophysical & Astrophysical Fluid Dynamics* **69**(1-4), 1–32.
- 453 Smyth, W. and Winters, K. (2003), ‘Turbulence and mixing in Holmboe waves’, *Journal of Phys-*
454 *ical Oceanography* **33**(4), 694–711.
- 455 Staquet, C. (1995), ‘Two-dimensional secondary instabilities in a strongly stratified shear layer’,
456 *Journal of Fluid Mechanics* **296**, 73–126.
- 457 Staquet, C. (2000), ‘Mixing in a stably stratified shear layer: two-and three-dimensional numerical
458 experiments’, *Fluid Dynamics Research* **27**(6), 367.
- 459 VanDine, A., Pham, H. T. and Sarkar, S. (2021), ‘Turbulent shear layers in a uniformly stratified
460 background: DNS at high reynolds number’, *Journal of Fluid Mechanics* **916**, A42.
- 461 Vreman, B., Geurts, B. and Kuerten, H. (1997), ‘Large-eddy simulation of the turbulent mixing
462 layer’, *Journal of Fluid Mechanics* **339**, 357–390.
- 463 Weinstock, J. (1978), ‘Vertical turbulent diffusion in a stably stratified fluid’, *Journal of Atmo-*
464 *spheric Sciences* **35**(6), 1022–1027.

- ⁴⁶⁵ Zhu, P. (2008), ‘Simulation and parameterization of the turbulent transport in the hurricane bound-
⁴⁶⁶ ary layer by large eddies’, *Journal of Geophysical Research: Atmospheres* **113**(D17).

467 LIST OF TABLES

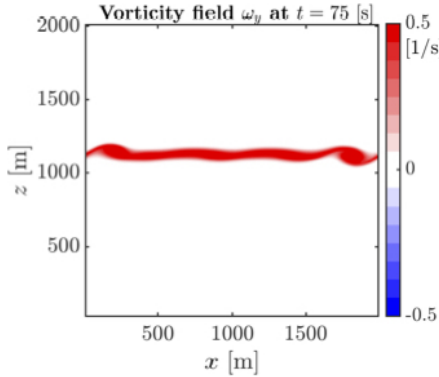
Simulations	$n_x \times n_y \times n_z$	$\mathcal{L}_x \times \mathcal{L}_y \times \mathcal{L}_z [\text{m}^3]$	Ri	$d [\text{m}]$	$\delta\theta/\theta_0$	$\mathcal{U} [\text{m/s}]$
Run # 1	$320 \times 320 \times 320$	$2000 \times 2000 \times 2000$	0.041	25	0.067	20
Run # 2	$320 \times 320 \times 320$	$2000 \times 2000 \times 2000$	0.082	50	0.067	20
Run # 3	$230 \times 230 \times 320$	$1438 \times 1438 \times 2000$	0.164	100	0.067	20
Run # 4	$230 \times 230 \times 320$	$1438 \times 1438 \times 2000$	0.197	100	0.067	18.20
Run # 5	$230 \times 230 \times 320$	$1438 \times 1438 \times 2000$	0.235	100	0.067	16.70
Run # 6	$230 \times 230 \times 320$	$1438 \times 1438 \times 2000$	0.327	100	0.067	14.14
Run # 7	$160 \times 160 \times 160$	$2000 \times 2000 \times 2000$	0.041	25	0.067	20
Run # 8	$80 \times 80 \times 80$	$2000 \times 2000 \times 2000$	0.041	25	0.067	20

TABLE 1: List of numerical simulations with LES.

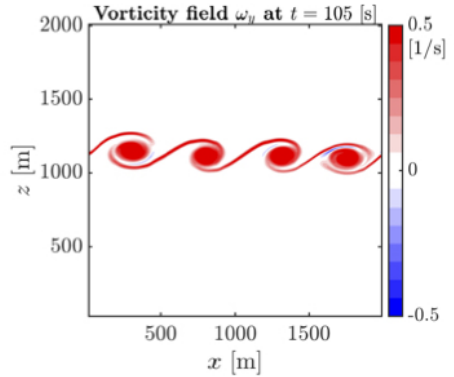
469 LIST OF FIGURES

470 Fig. 1. Time evolution of vorticity field in the x - z plane at $y \approx 500$ [m] for the case with the initial 471 bulk Richardson number $Ri = 0.041$ and shear layer thickness $d = 25$ [m].	30
472 Fig. 2. Time evolution of vorticity field in the x - z plane at $y \approx 500$ [m] for the case with the initial 473 bulk Richardson number $Ri = 0.082$ and shear layer thickness $d = 50$ [m]. See also figure 3 474 for plots in the x - y and y - z planes.	31
475 Fig. 3. Time evolution of vorticity field ω_y in the (left) x - y plane at $z \approx 1200$ [m] and (right) y - z 476 plane $x \approx 500$ [m] at for the case with the initial bulk Richardson number $Ri = 0.082$ and 477 shear layer thickness $d = 50$ [m]. Plots in the x - z plane are shown in figure 2.	32
478 Fig. 4. Time evolution of vorticity field in the x - z plane at $y \approx 500$ [m] for the case with the initial 479 bulk Richardson number $Ri = 0.164$ and shear layer thickness $d = 100$ [m].	33
480 Fig. 5. The vorticity field in the x - z plane at $y \approx 500$ [m] for cases with the initial bulk Richardson 481 number (a) $Ri = 0.197$ and (b) $Ri = 0.235$, and shear layer thickness $d = 100$ [m].	34
482 Fig. 6. Time evolution of vertically-averaged horizontal kinetic and available potential energy spec- 483 tra for the case with the initial bulk Richardson number $Ri = 0.041$ and shear layer thickness 484 $d = 25$ [m]. Spectra are averaged over the mixed layer height (between $z \approx 710$ and 1460 485 [m]).	35
486 Fig. 7. Time evolution of vertically-averaged horizontal kinetic and available potential energy spec- 487 tra for the case with the initial bulk Richardson number $Ri = 0.082$ and shear layer thickness 488 $d = 50$ [m]. Spectra are averaged over the mixed layer height.	36
489 Fig. 8. Vertically-averaged horizontal kinetic and available potential energy spectra at time (a) $t =$ 490 525 and (b) $t = 795$ [s], for the case with the initial bulk Richardson number $Ri = 0.164$ and 491 shear layer thickness $d = 100$ [m]. Spectra are averaged over the mixed layer height.	37
492 Fig. 9. Vertically-averaged horizontal kinetic and available potential energy spectra at time (a) $t =$ 493 585 and (b) $t = 885$ [s], for the case with the initial bulk Richardson number $Ri = 0.197$ and 494 shear layer thickness $d = 100$ [m]. Spectra are averaged over the mixed layer height.	38
495 Fig. 10. Time evolution of resolved shear characteristics $\bar{S} = (G_{ij}G_{ij})^{1/4}$ in the x - z plane at $y \approx 500$ 496 [m] for the case with the initial bulk Richardson number $Ri = 0.041$ and shear layer thickness 497 $d = 25$ [m].	39
498 Fig. 11. Time evolution of the scatter diagram of vorticity field ω_y versus the resolved shear \bar{S} for the 499 case with the initial bulk Richardson number $Ri = 0.041$ and shear layer thickness $d = 25$ 500 [m]. Lines $\omega_y = \pm \bar{S}$ are shown for references.	40
502 Fig. 12. Time evolution of kinetic energy eddy dissipation rate $\varepsilon = 2v_g s_{ij} s_{ij}$ in the x - z plane at $y \approx$ 503 500 [m] for the case with the initial bulk Richardson number $Ri = 0.041$ and shear layer thickness $d = 25$ [m].	41
504 Fig. 13. Time evolution of potential energy eddy dissipation rate $\varepsilon_p = Ri D_g (\partial \bar{\theta} / \partial x_j) (\partial \bar{\theta} / \partial x_j)$ in 505 the x - z plane at $y \approx 500$ [m] for the case with the initial bulk Richardson number $Ri = 0.041$ 506 and shear layer thickness $d = 25$ [m]. Note that $D_g = v_g / Pr_t$	42

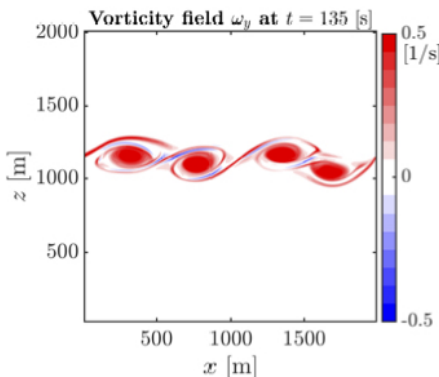
507	Fig. 14. Time evolution of resolved shear characteristics $\bar{S} = (G_{ij}G_{ij})^{1/4}$ in the x - z plane at $y \approx 500$ [m] for the case with the initial bulk Richardson number $Ri = 0.082$ and shear layer thickness $d = 50$ [m].	43
510	Fig. 15. (a,b) Kinetic energy eddy dissipation rate $\varepsilon = 2v_g s_{ij} s_{ij}$ and (c,d) potential energy eddy dissipation rate $\varepsilon_p = Ri D_g (\partial \bar{\theta} / \partial x_j) (\partial \bar{\theta} / \partial x_j)$ in the x - z plane at $y \approx 500$ [m] for the case with the initial bulk Richardson number $Ri = 0.082$ and shear layer thickness $d = 50$ [m]. Note that $D_g = v_g / Pr_t$	44
514	Fig. 16. (a) Kinetic energy eddy dissipation rate $\varepsilon = 2v_g s_{ij} s_{ij}$ and (b) potential energy eddy dissipation rate $\varepsilon_p = Ri D_g (\partial \bar{\theta} / \partial x_j) (\partial \bar{\theta} / \partial x_j)$ in the x - z plane at $y \approx 500$ [m] for the case with the initial bulk Richardson number $Ri = 0.164$ and shear layer thickness $d = 100$ [m]. Note that $D_g = v_g / Pr_t$	45
518	Fig. 17. Potential energy eddy dissipation rate $\varepsilon_p = Ri D_g (\partial \bar{\theta} / \partial x_j) (\partial \bar{\theta} / \partial x_j)$ in the x - z plane at $y \approx 500$ [m] for the case with the initial bulk Richardson number $Ri = 0.197$ and shear layer thickness $d = 100$ [m]. Note that $D_g = v_g / Pr_t$	46
521	Fig. 18. Time evolution of irreversible mixing efficiency γ_i in the x - z plane at $y \approx 500$ [m] for the case with the initial bulk Richardson number $Ri = 0.041$ and shear layer thickness $d = 25$ [m].	47
524	Fig. 19. Time evolution of vorticity field in the x - z plane at $y \approx 500$ [m] when (a) $t = 945$ and (b) $t = 1125$ [s] for the case with the initial bulk Richardson number $Ri = 0.164$ and shear layer thickness $d = 100$ [m], when the Smagorinsky parameterization is employed. (c) kinetic and (d) potential eddy dissipation rates at $t = 1185$ [s].	48



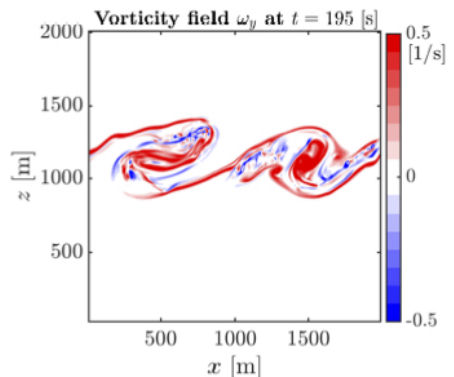
(a) $t = 75$ [s]



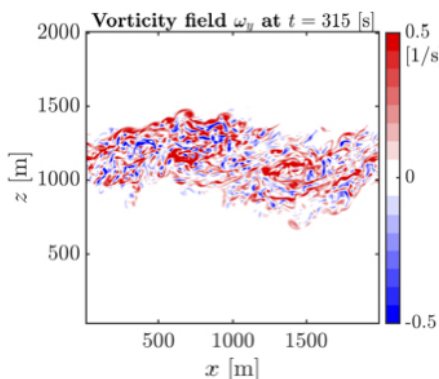
(b) $t = 105$ [s]



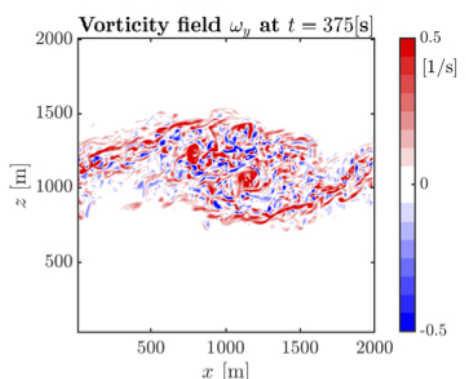
(c) $t = 135$ [s]



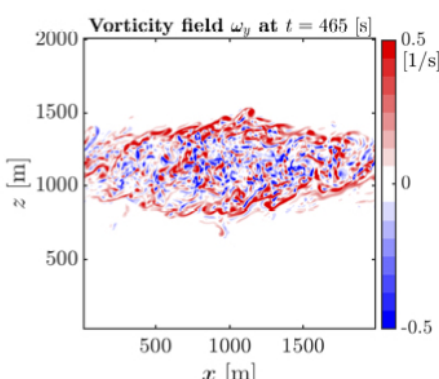
(d) $t = 195$ [s]



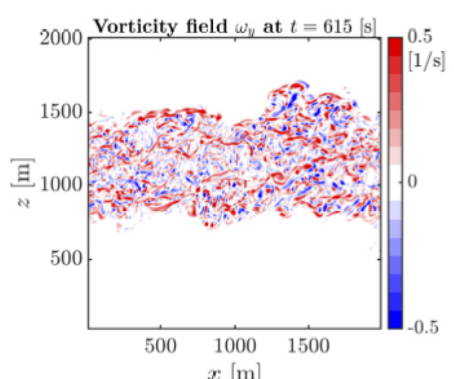
(e) $t = 315$ [s]



(f) $t = 375$ [s]



(g) $t = 465$ [s]



(h) $t = 615$ [s]

FIG. 1: Time evolution of vorticity field in the x - z plane at $y \approx 500$ [m] for the case with the initial bulk Richardson number $Ri = 0.041$ and shear layer thickness $d = 25$ [m].

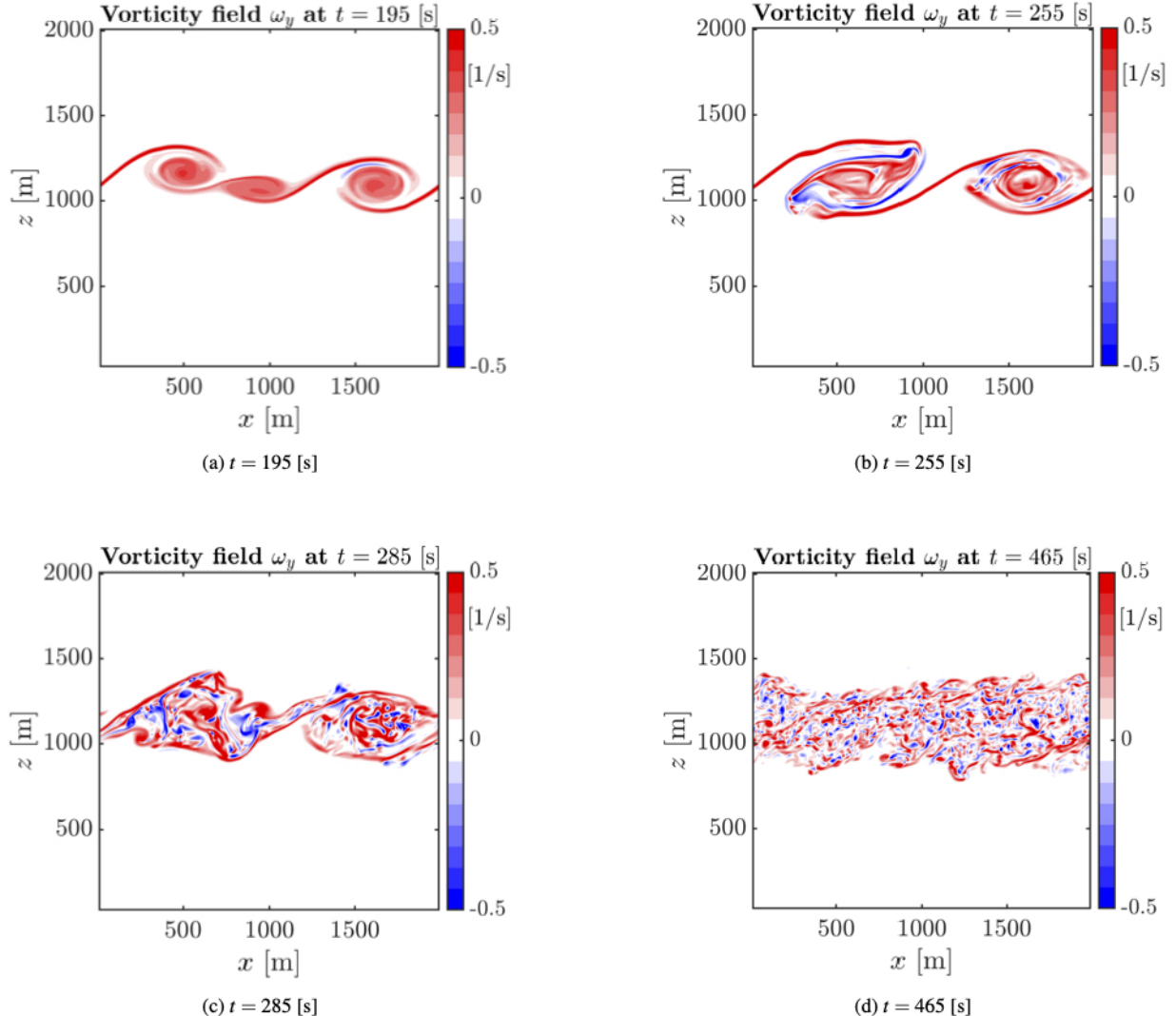


FIG. 2: Time evolution of vorticity field in the x - z plane at $y \approx 500$ [m] for the case with the initial bulk Richardson number $Ri = 0.082$ and shear layer thickness $d = 50$ [m]. See also figure 3 for plots in the x - y and y - z planes.

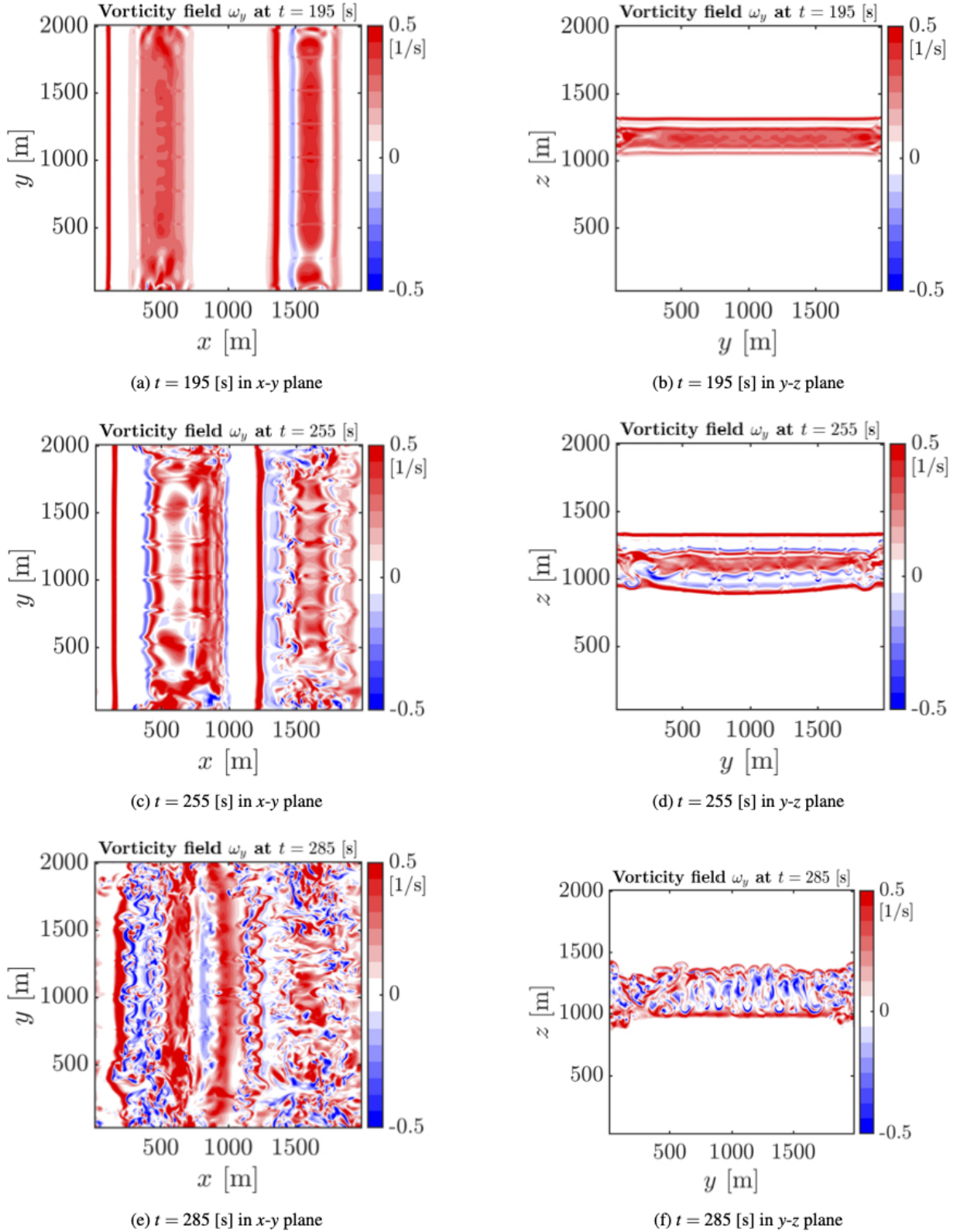


FIG. 3: Time evolution of vorticity field ω_y in the (left) x - y plane at $z \approx 1200$ [m] and (right) y - z plane $x \approx 500$ [m] at for the case with the initial bulk Richardson number $Ri = 0.082$ and shear layer thickness $d = 50$ [m]. Plots in the x - z plane are shown in figure 2.

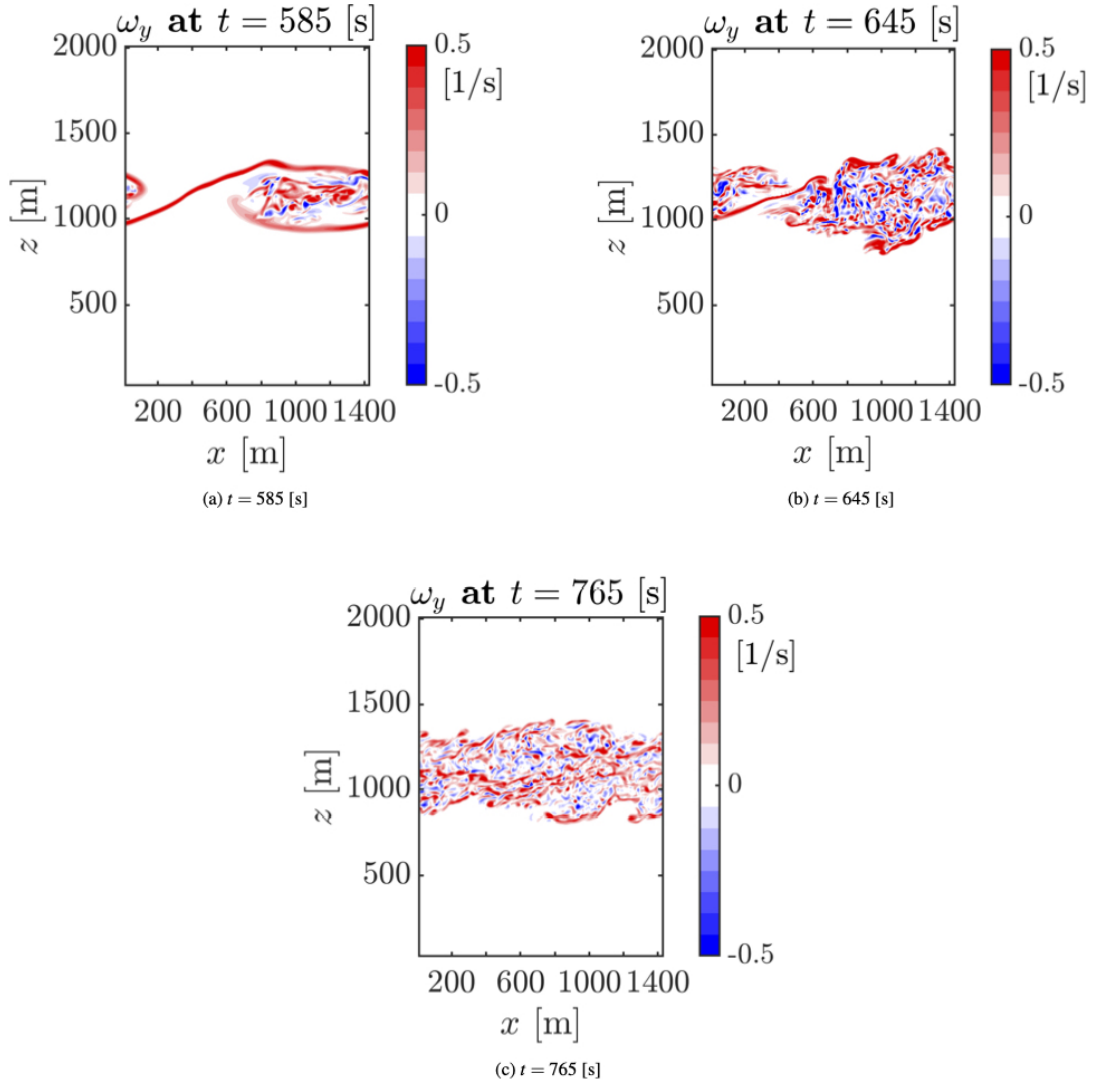


FIG. 4: Time evolution of vorticity field in the x - z plane at $y \approx 500$ [m] for the case with the initial bulk Richardson number $Ri = 0.164$ and shear layer thickness $d = 100$ [m].

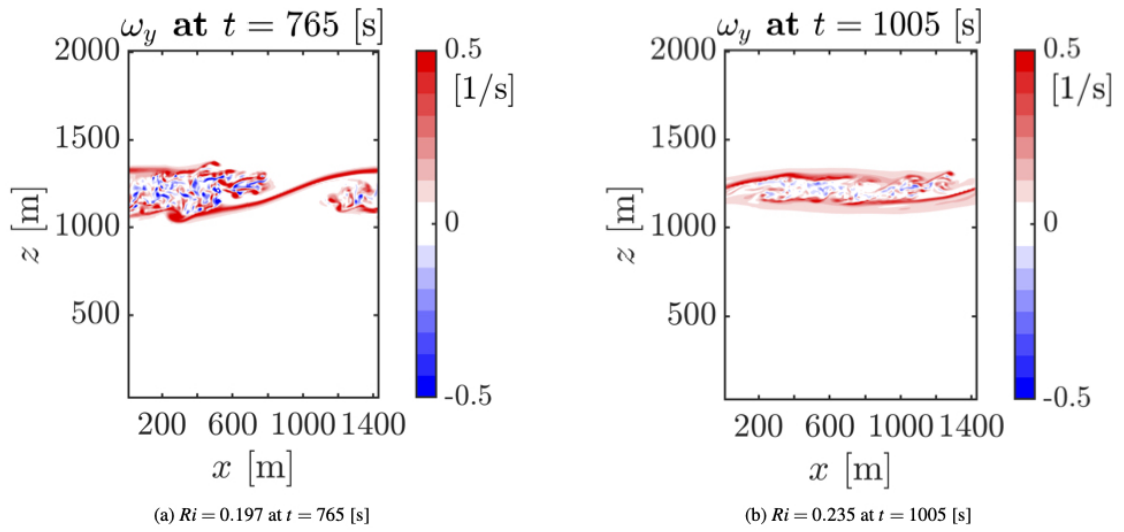


FIG. 5: The vorticity field in the x - z plane at $y \approx 500$ [m] for cases with the initial bulk Richardson number (a) $Ri = 0.197$ and (b) $Ri = 0.235$, and shear layer thickness $d = 100$ [m].

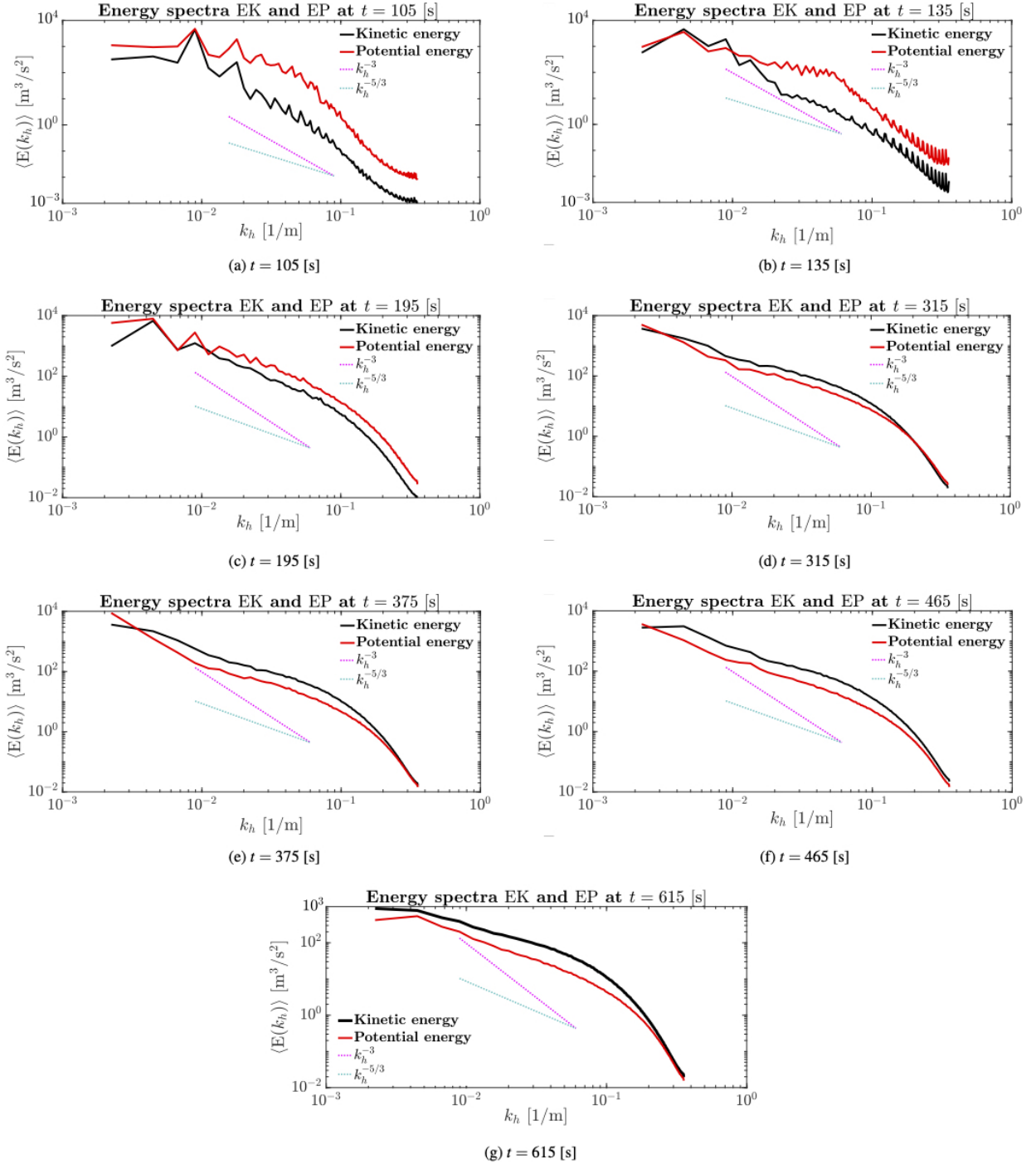


FIG. 6: Time evolution of vertically-averaged horizontal kinetic and available potential energy spectra for the case with the initial bulk Richardson number $Ri = 0.041$ and shear layer thickness $d = 25$ [m]. Spectra are averaged over the mixed layer height (between $z \approx 710$ and 1460 [m]).

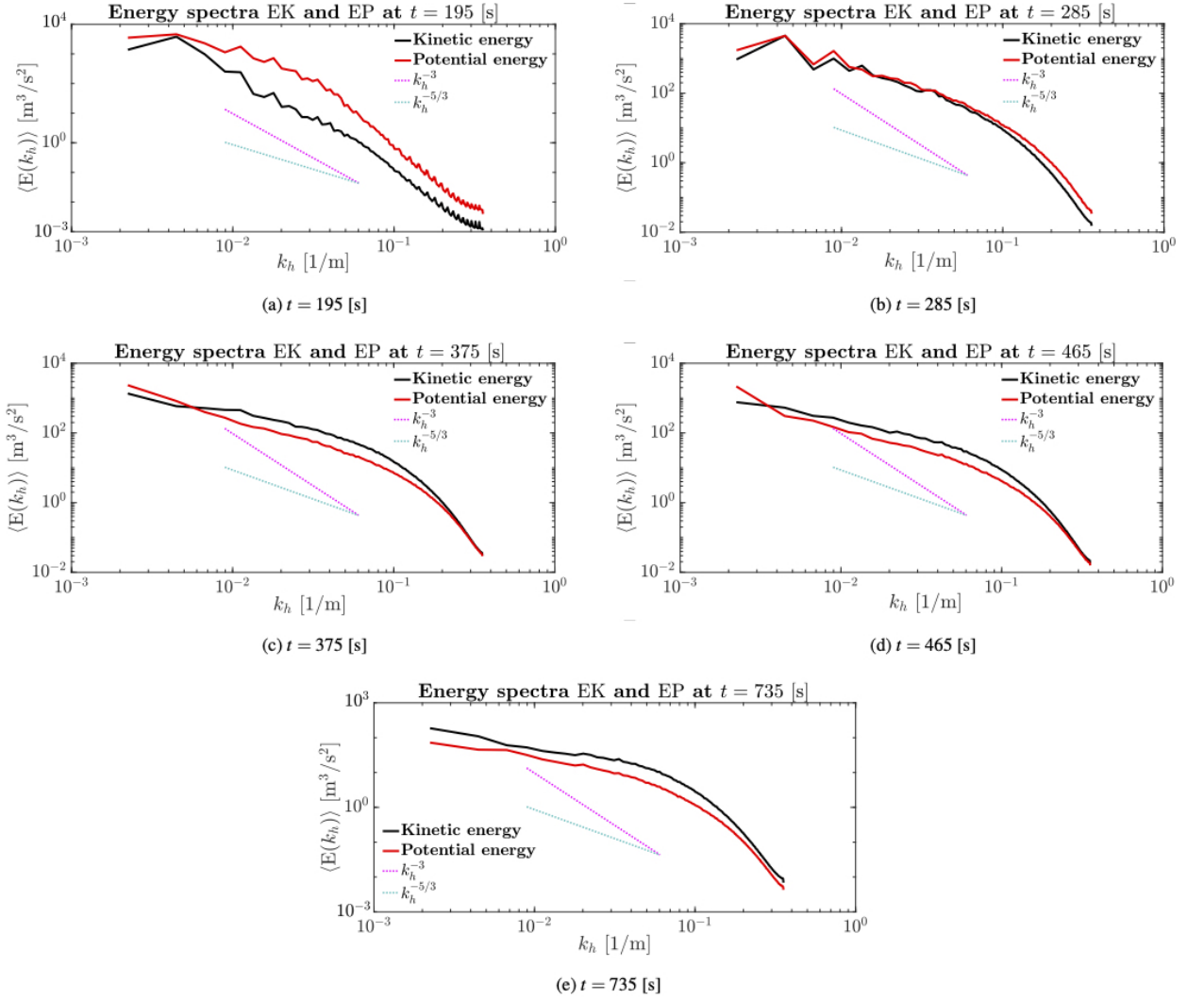


FIG. 7: Time evolution of vertically-averaged horizontal kinetic and available potential energy spectra for the case with the initial bulk Richardson number $\text{Ri} = 0.082$ and shear layer thickness $d = 50$ [m]. Spectra are averaged over the mixed layer height.

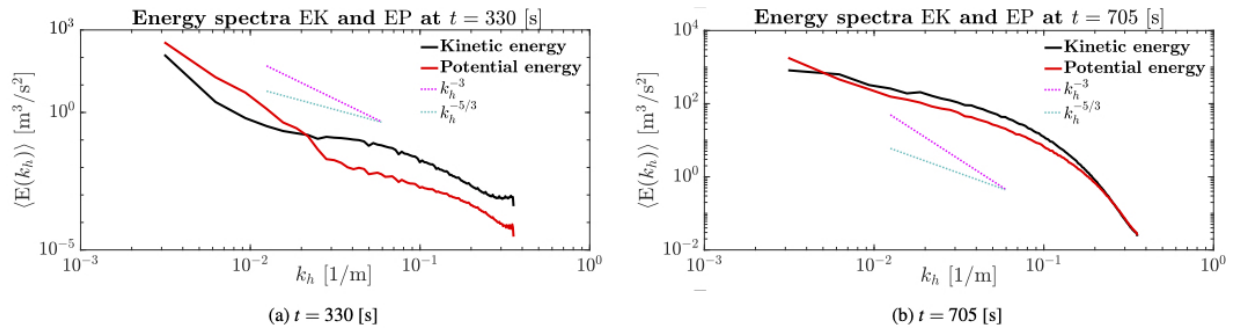


FIG. 8: Vertically-averaged horizontal kinetic and available potential energy spectra at time (a) $t = 525$ and (b) $t = 795$ [s], for the case with the initial bulk Richardson number $\text{Ri} = 0.164$ and shear layer thickness $d = 100$ [m]. Spectra are averaged over the mixed layer height.

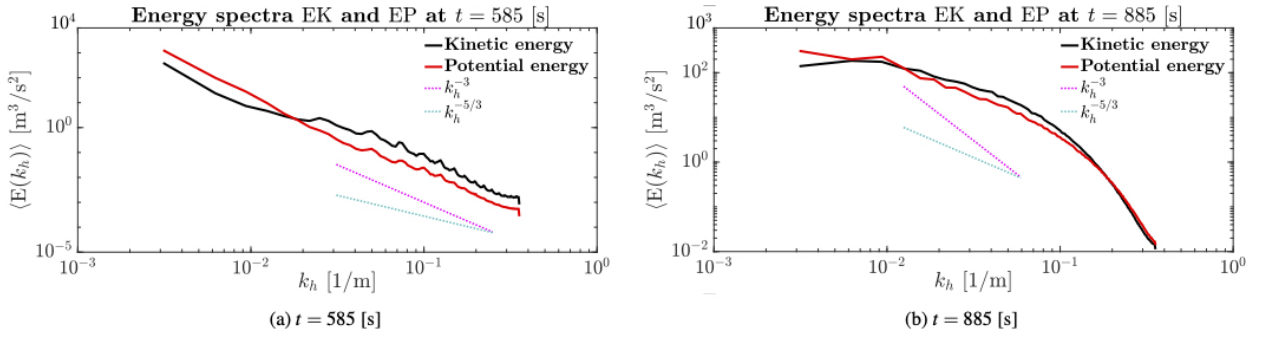


FIG. 9: Vertically-averaged horizontal kinetic and available potential energy spectra at time (a) $t = 585$ [s] and (b) $t = 885$ [s], for the case with the initial bulk Richardson number $Ri = 0.197$ and shear layer thickness $d = 100$ [m]. Spectra are averaged over the mixed layer height.

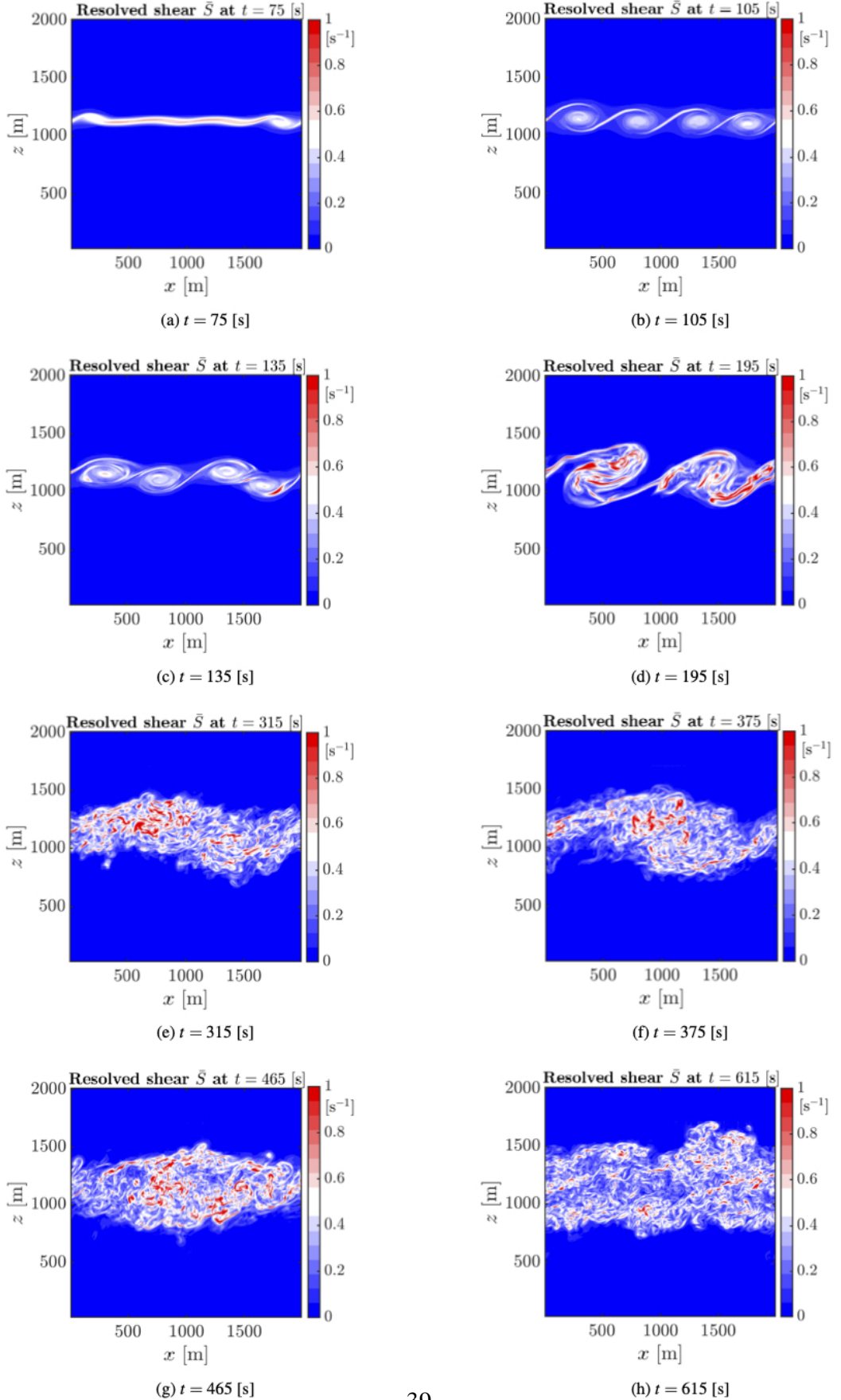


FIG. 10: Time evolution of resolved shear characteristics $\bar{S} = (G_{ij}G_{ij})^{1/4}$ in the x - z plane at $y \approx 500$ [m] for the case with the initial bulk Richardson number $Ri = 0.041$ and shear layer thickness $d = 25$ [m].

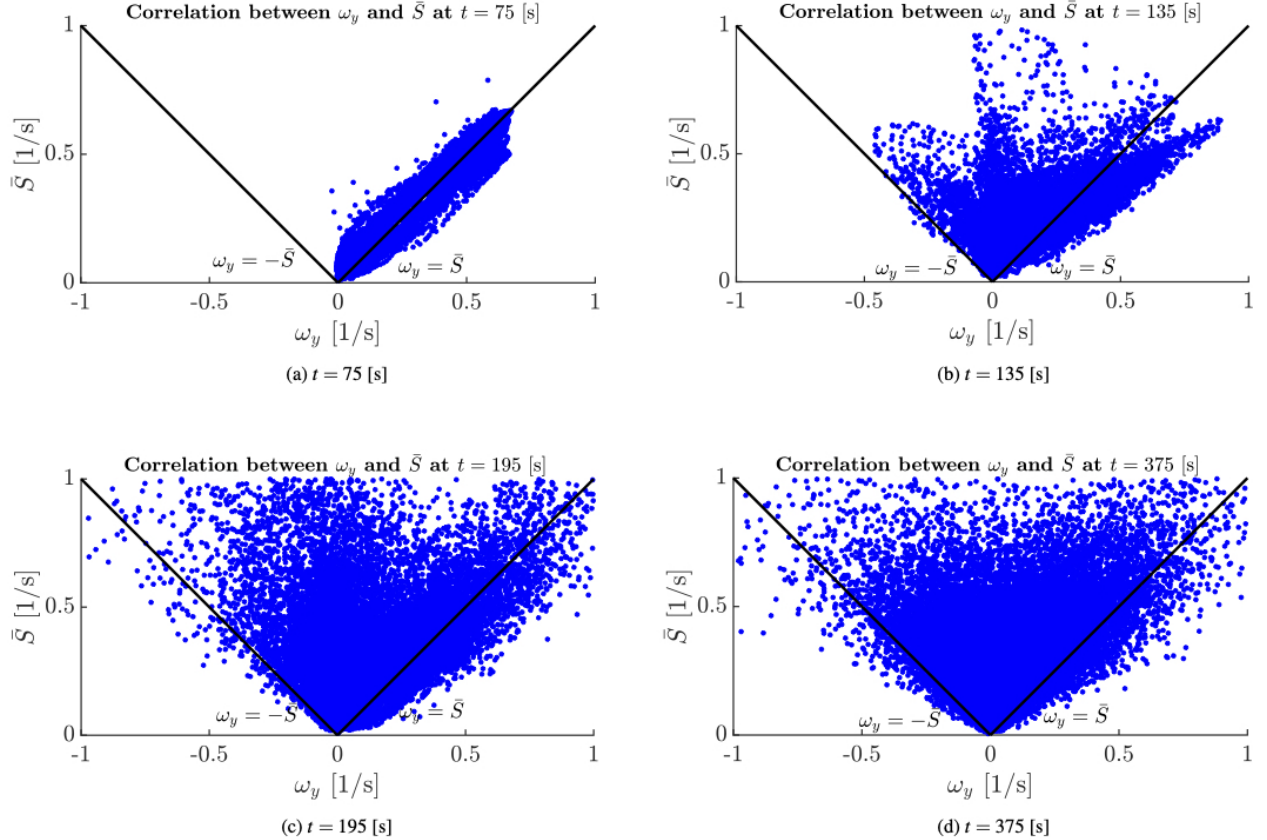


FIG. 11: Time evolution of the scatter diagram of vorticity field ω_y versus the resolved shear \bar{S} for the case with the initial bulk Richardson number $Ri = 0.041$ and shear layer thickness $d = 25$ [m]. Lines $\omega_y = \pm \bar{S}$ are shown for references.

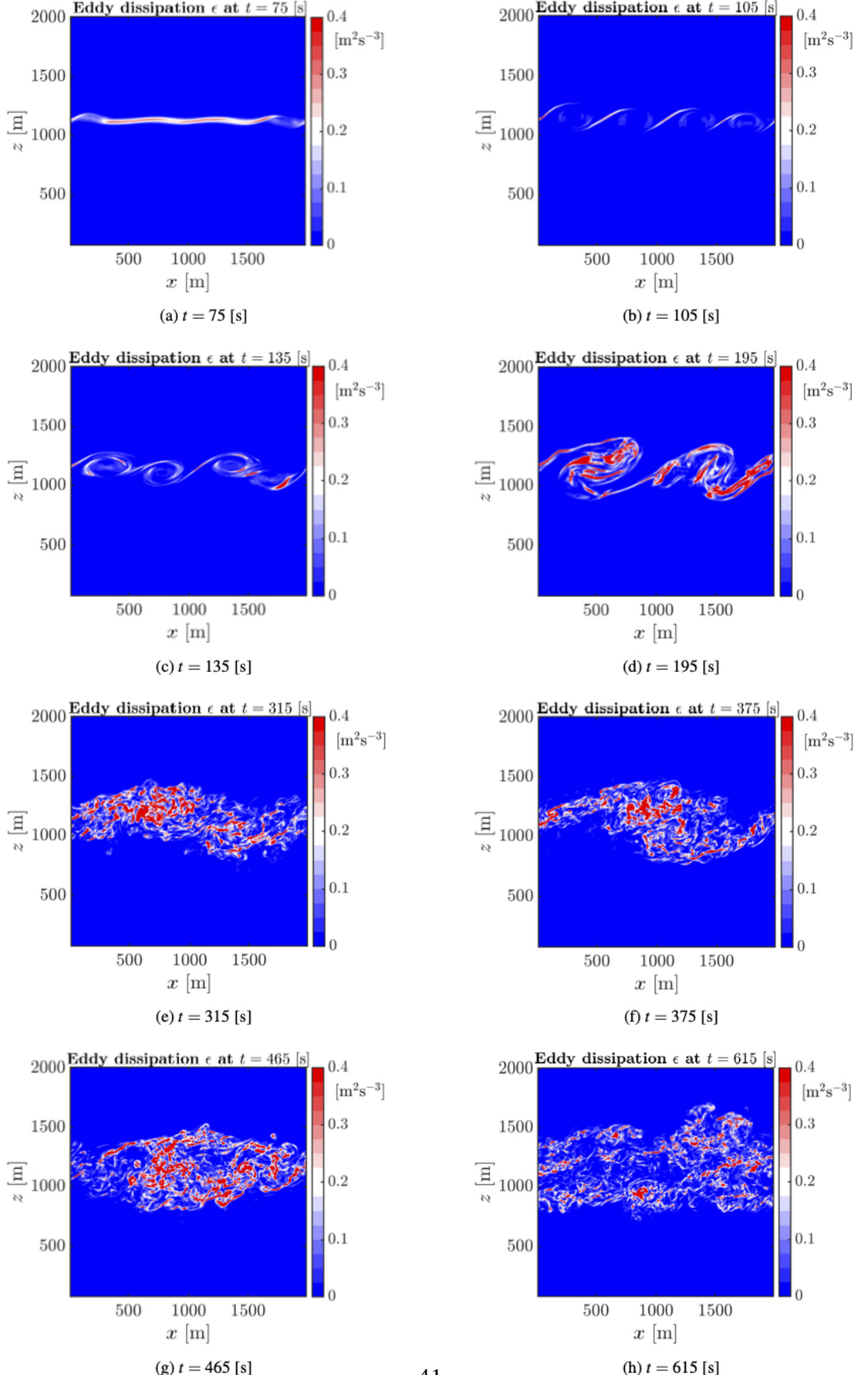


FIG. 12: Time evolution of kinetic energy eddy dissipation rate $\epsilon = 2v_g s_{ij} s_{ij}$ in the x - z plane at $y \approx 500$ [m] for the case with the initial bulk Richardson number $Ri = 0.041$ and shear layer thickness $d = 25$ [m].

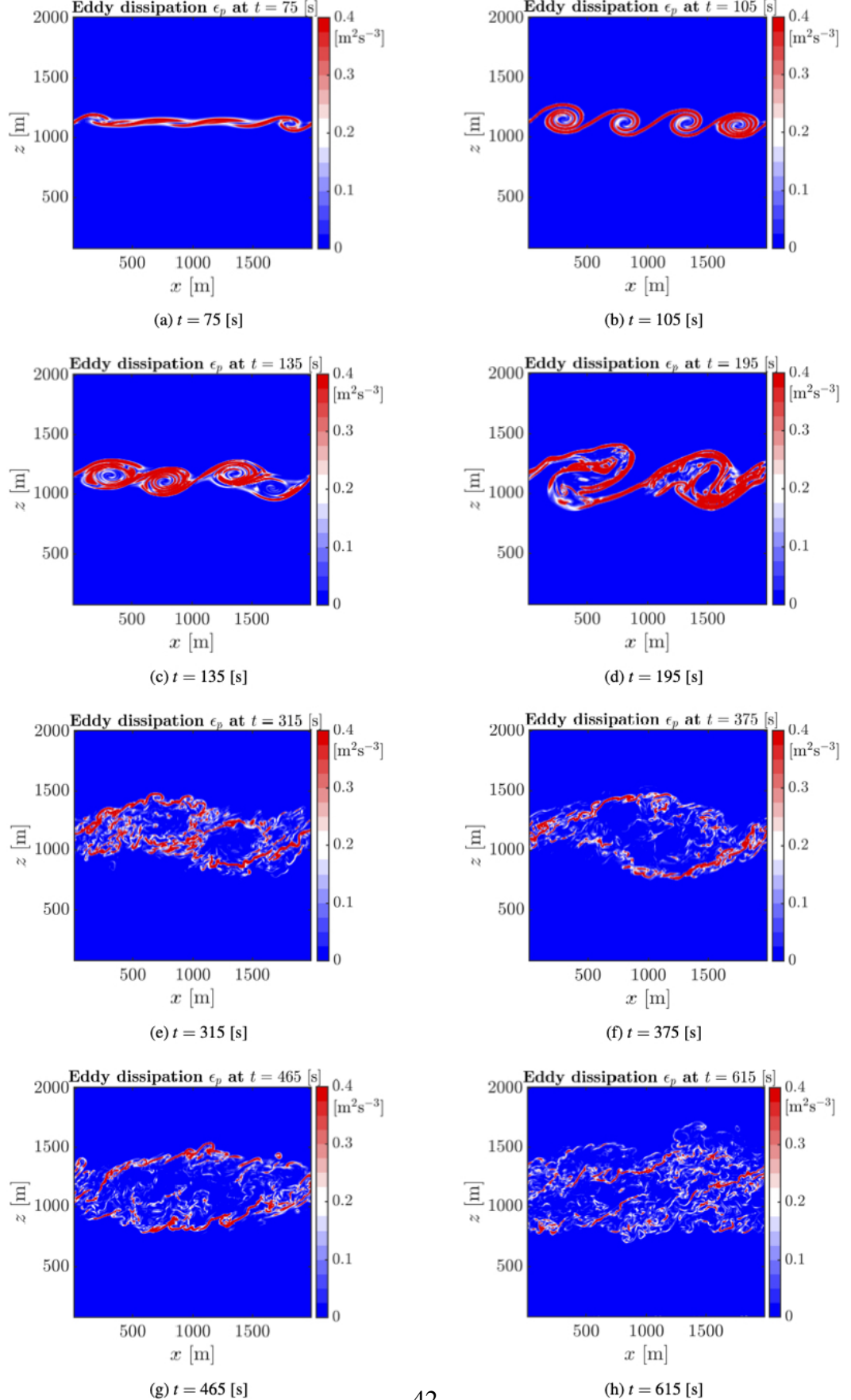


FIG. 13: Time evolution of potential energy eddy dissipation rate $\epsilon_p = \text{Ri} D_g (\partial \bar{\theta} / \partial x_j) (\partial \bar{\theta} / \partial x_j)$ in the x - z plane at $y \approx 500$ [m] for the case with the initial bulk Richardson number $\text{Ri} = 0.041$ and shear layer thickness $d = 25$ [m]. Note that $D_g = v_g / Pr_t$.

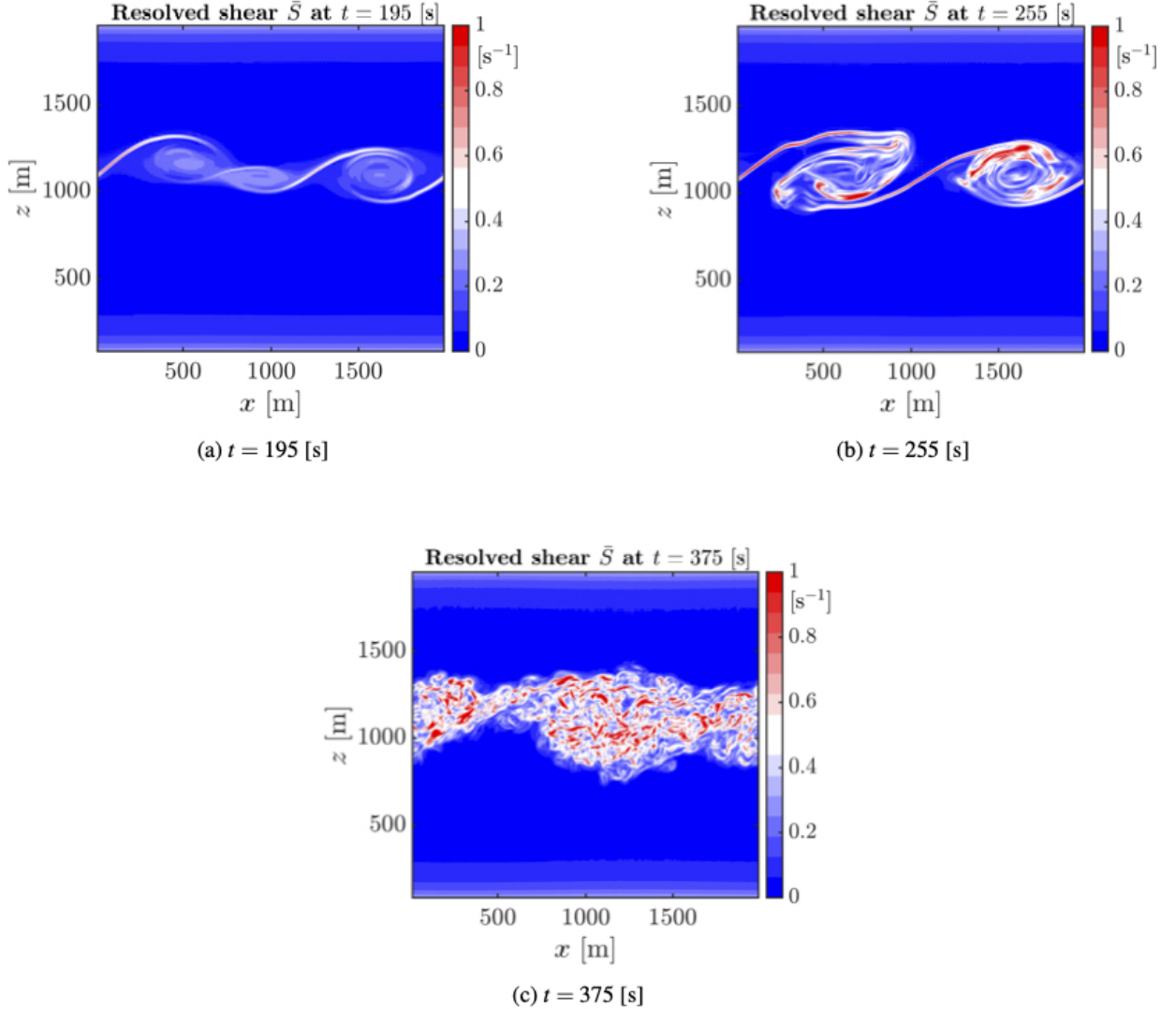


FIG. 14: Time evolution of resolved shear characteristics $\bar{S} = (G_{ij}G_{ij})^{1/4}$ in the x - z plane at $y \approx 500$ [m] for the case with the initial bulk Richardson number $\text{Ri} = 0.082$ and shear layer thickness $d = 50$ [m].

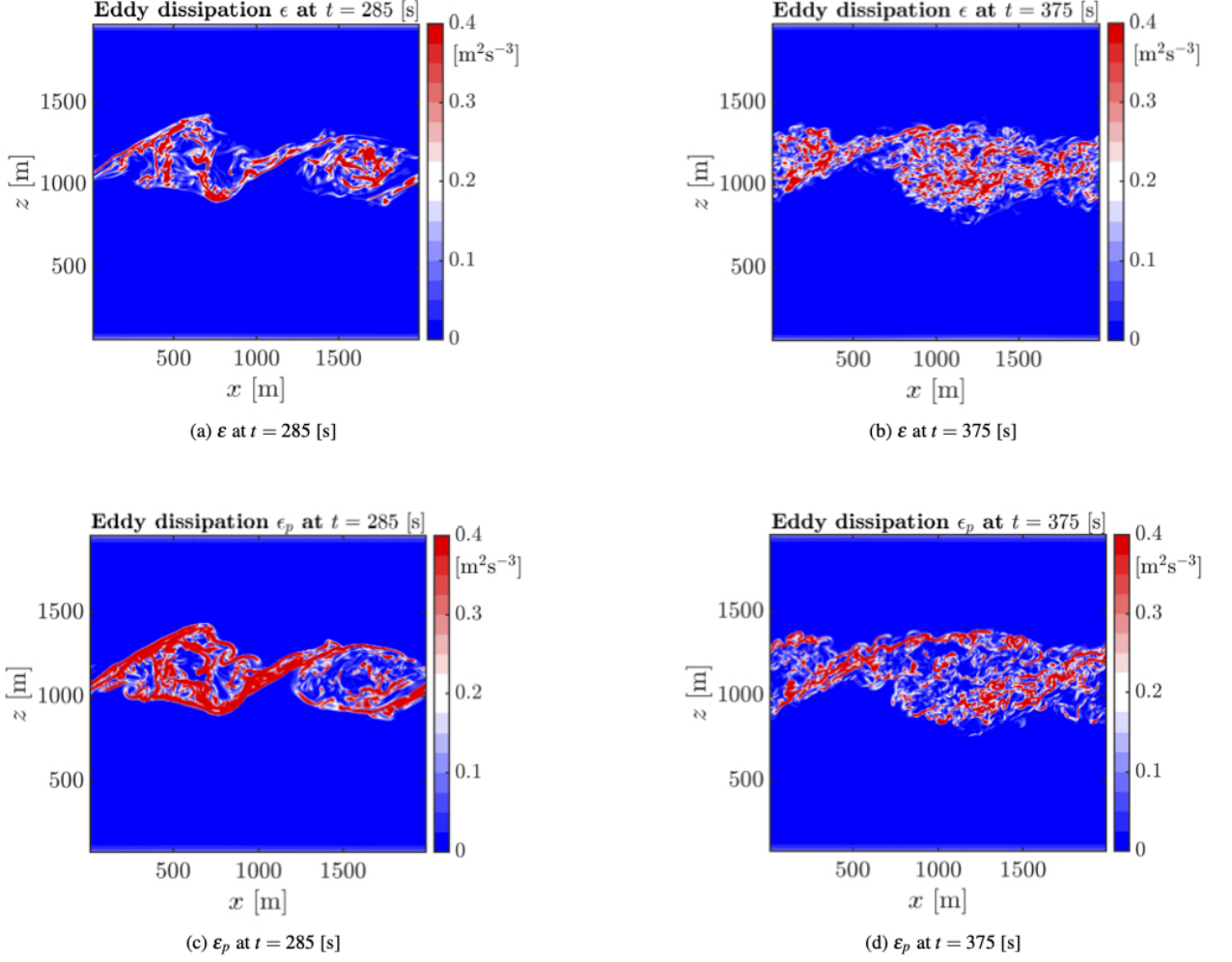


FIG. 15: (a,b) Kinetic energy eddy dissipation rate $\epsilon = 2v_g s_{ij} s_{ij}$ and (c,d) potential energy eddy dissipation rate $\epsilon_p = \text{Ri} D_g (\partial \bar{\theta} / \partial x_j) (\partial \bar{\theta} / \partial x_i)$ in the x - z plane at $y \approx 500$ [m] for the case with the initial bulk Richardson number $\text{Ri} = 0.082$ and shear layer thickness $d = 50$ [m]. Note that $D_g = v_g / Pr_t$.

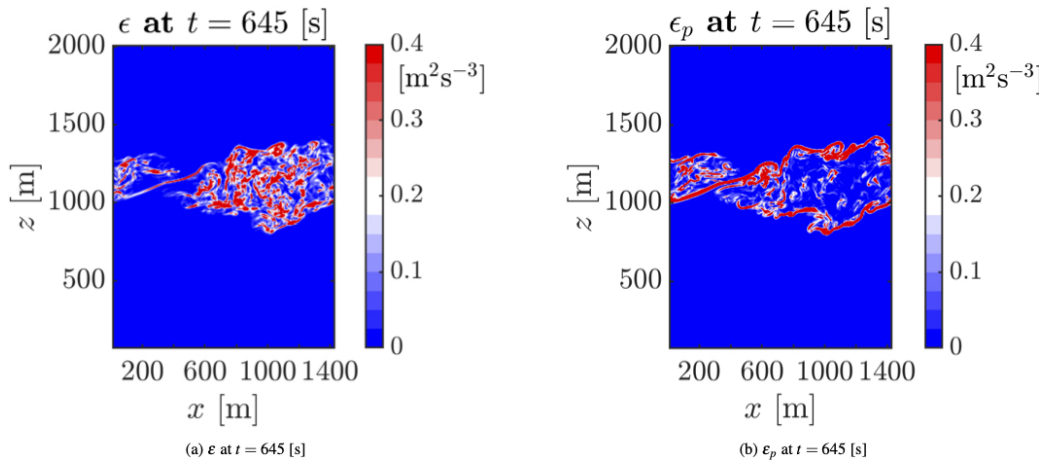


FIG. 16: (a) Kinetic energy eddy dissipation rate $\epsilon = 2v_g s_{ij} s_{ij}$ and (b) potential energy eddy dissipation rate $\epsilon_p = \text{Ri} D_g (\partial \bar{\theta} / \partial x_j) (\partial \bar{\theta} / \partial x_i)$ in the x - z plane at $y \approx 500$ [m] for the case with the initial bulk Richardson number $\text{Ri} = 0.164$ and shear layer thickness $d = 100$ [m]. Note that $D_g = v_g / Pr_t$.

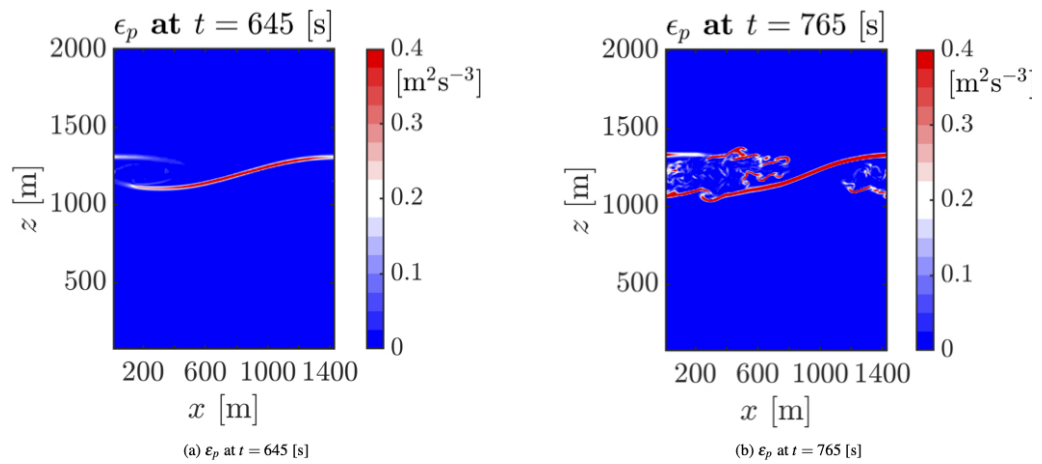


FIG. 17: Potential energy eddy dissipation rate $\epsilon_p = \text{Ri} D_g (\partial \bar{\theta} / \partial x_j) (\partial \bar{\theta} / \partial x_j)$ in the x - z plane at $y \approx 500$ [m] for the case with the initial bulk Richardson number $\text{Ri} = 0.197$ and shear layer thickness $d = 100$ [m]. Note that $D_g = v_g / Pr_t$.

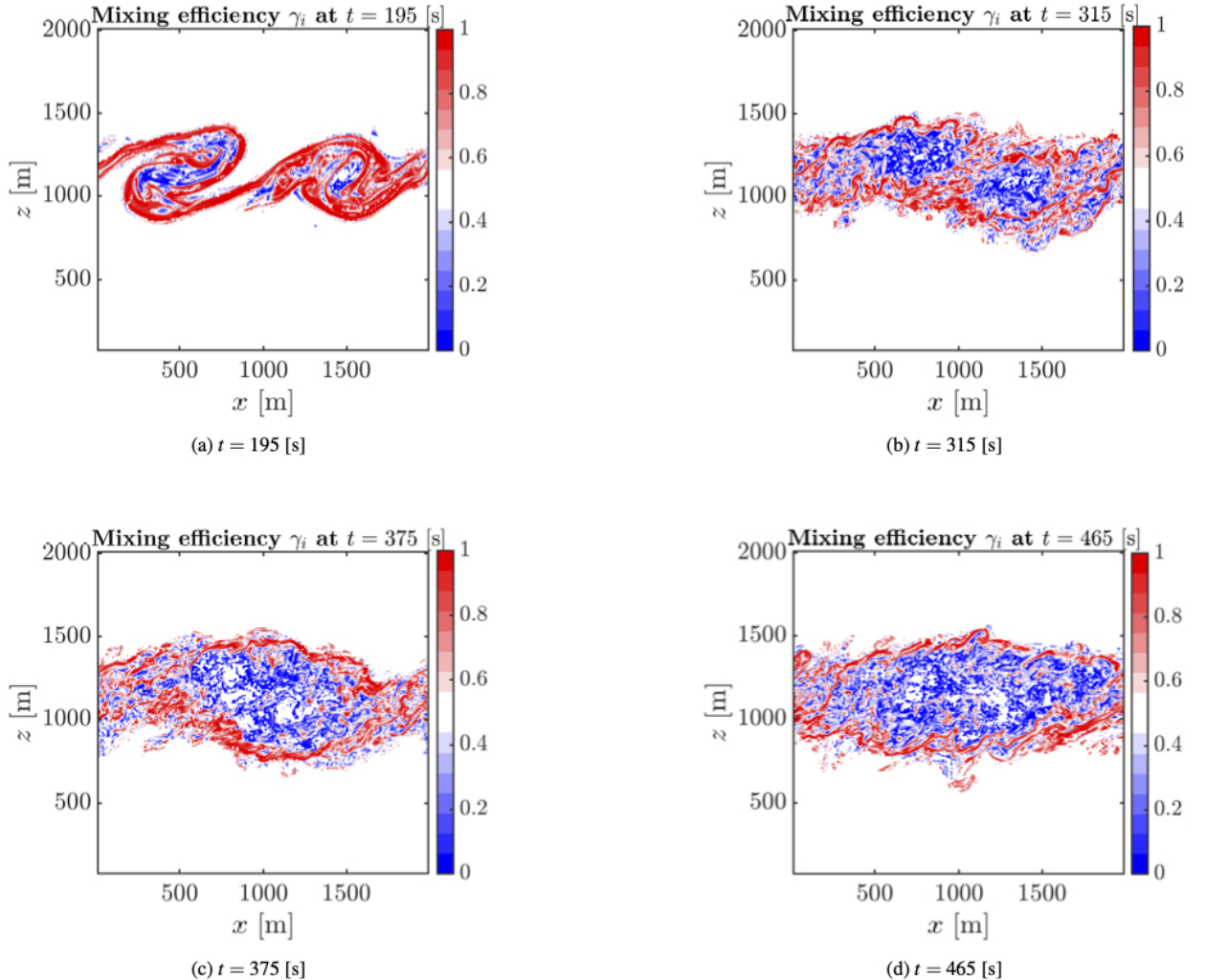


FIG. 18: Time evolution of irreversible mixing efficiency γ in the x - z plane at $y \approx 500$ [m] for the case with the initial bulk Richardson number $Ri = 0.041$ and shear layer thickness $d = 25$ [m].

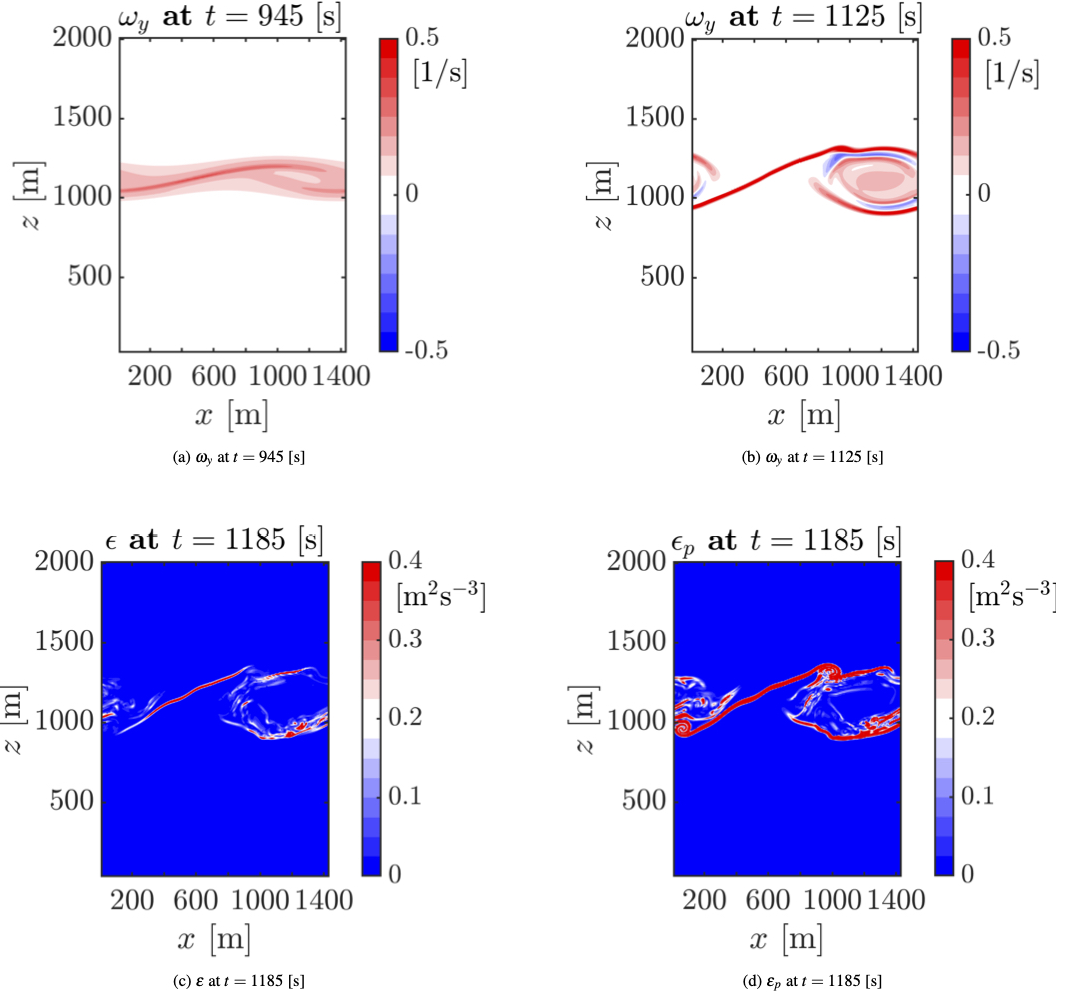


FIG. 19: Time evolution of vorticity field in the x - z plane at $y \approx 500$ [m] when (a) $t = 945$ and (b) $t = 1125$ [s] for the case with the initial bulk Richardson number $\text{Ri} = 0.164$ and shear layer thickness $d = 100$ [m], when the Smagorinsky parameterization is employed. (c) kinetic and (d) potential eddy dissipation rates at $t = 1185$ [s].